

THE NEAR STELLAR ENVIRONMENT OF CLASS 0 PROTOSTARS: A FIRST LOOK WITH NEAR-INFRARED SPECTROSCOPY

STEFAN LAOS¹, THOMAS P. GREENE², JOAN R. NAJITA³, AND KEIVAN G. STASSUN¹

Draft version August 24, 2021

ABSTRACT

We present near-infrared K -band spectra for a sample of 7 Class 0 protostars in the Perseus and Orion star-forming regions. We detect Br γ , CO overtone, and H₂ emission, features that probe the near circumstellar environment of the protostar and reveal evidence of magnetospheric accretion, a hot inner disk atmosphere, and outflows, respectively. Comparing the properties of these features with those of Class I sources from the literature, we find that their Br γ and CO emission are generally consistent in strength and velocity width. The Br γ line profiles are broad and centrally peaked, with FWHMs of ~ 200 km s⁻¹ and wings extending to ~ 300 km s⁻¹. The line ratios of our H₂ emission features, which are spatially extended for some sources, are consistent with shock excitation and indicate the presence of strong jets or a disk wind. Within our small sample, the frequency of CO band emission ($\sim 67\%$) is high relative to that of Class I samples ($\sim 15\%$), indicating that Class 0s have high inner disk accretion rates, similar to those of the most actively accreting Class I sources. Collectively, our results suggest that Class 0 sources have similar accretion mechanisms to the more evolved classes, with strong organized stellar magnetic fields established at the earliest observable stage of evolution.

1. INTRODUCTION

Numerous strides have been made over the past decades to understand the mass accretion of young stellar objects (YSOs), both from an observational and modeling perspective. By the ages of ~ 1 – 10 Myr, YSOs fall into the class of T Tauri stars (TTs, Class II/III). Their dissipated envelopes have allowed for detailed study in both the near-infrared (NIR) and visible. Overall, these phases mark the end of the mass accretion phase, with only the most active Class IIs exhibiting ongoing accretion.

At the age of ~ 0.5 Myr, the earlier stage of Class I protostars are believed to be actively accreting, in the process of building toward their final stellar mass from the reservoir of material in their surrounding envelopes (Dunham et al. 2014). Sensitive array (SMA, ALMA, NOEMA) observations in the millimeter regime have detected these massive envelopes (Jørgensen et al. 2009) and used the molecular line emission from their circumstellar disks to place dynamical constraints on the masses of these protostars (Harsono et al. 2014, Yen et al. 2017, Aso et al. 2017, Maret et al. 2020, Tobin et al. 2020a, Reynolds et al. 2021). Additionally, near-infrared observations have given us further insight into the embedded central stars, in some cases detecting photospheric absorption features and emission features (Doppmann et al. 2005, Connelley & Greene 2010) that confirm active accretion.

In the past decades, the advent of sensitive, all-sky mid-infrared observatories (*IRAS*, *Spitzer*, *Herschel*) has revealed over a hundred systems younger than Class Is,

designated as Class 0 protostars, in nearby dark clouds. Mounting evidence has found these Class 0s have similar system morphologies to that of the more evolved classes at large scales. Class 0s also exhibit massive surrounding envelopes and energetic, high-velocity outflows (Andre et al. 1993), likely powered by strong mass accretion. Recent millimeter observations have begun to reveal the presence of small (on average ~ 40 AU) circumstellar disks around a fraction of Class 0 objects (Tobin et al. 2013, Segura-Cox et al. 2018, Maury et al. 2019, Tobin et al. 2020b).

These Class 0 protostars are also thought to be actively accreting, with the majority of their final stellar mass still in the surrounding envelope. Statistical analyses of large YSO samples support a relatively short duration for the Class 0 phase, with lifetimes of ~ 0.1 – 0.2 Myr (Dunham et al. 2015). This brief evolutionary stage likely corresponds to the highest level of overall stellar mass accretion in these objects. Growing evidence finds this accretion is episodic to a degree, with outflow clump structure (Arce & Goodman 2001, Plunkett et al. 2015) and CO₂ ice features (Dunham et al. 2014) documenting outburst history as frequent and variable.

Historically, however, high visual extinctions ($A_V \geq 70$) have made detailed study of the Class 0 central stars difficult. High sensitivity observations are required to analyze the, often scattered, near-IR light that leaks through less dense parts of the envelope and the outflow cavities. As a result, little is known about the underlying mechanisms governing young stellar mass accretion and the extent to which they differ between the evolutionary classes. In particular, it is still unclear how nascent protostars manage their angular momentum budget during their formation.

As they accrete increasingly high angular momentum material from their molecular envelopes, protostars can eventually be spun up to breakup rotational velocities in the absence of an efficient angular momentum loss

¹ Department of Physics and Astronomy, Vanderbilt University, Nashville, TN 37235, USA

² NASA Ames Research Center Space Science and Astrobiology Division M.S. 245-6 Moffett Field, CA 94035, USA

³ National Optical Astronomy Observatory, 950 N. Cherry Avenue, Tucson, AZ 85719, USA

mechanism. For example, in the idealized case of infall from a singular isothermal sphere with molecular core angular rotation rates of a few times 10^{-14} s^{-1} , breakup velocities are reached at a small fraction of a solar mass, $\sim 0.2 M_{\odot}$ (Durisen et al. 1989, Tobin et al. 2012). This mass regime likely corresponds to the Class 0 or early Class I phase for a final star of moderate mass ($\sim 0.5\text{--}1 M_{\odot}$) given typical accretion rates and lifetimes of the different protostellar stages (e.g. the estimated Class 0 lifetime of $\sim 0.2 \text{ Myr}$ with an accretion rate of $\sim 10^{-6} M_{\odot}/\text{yr}$).

One proposed mechanism to accrete past this expected mass limit is by launching a powerful stellar wind that removes angular momentum and drives molecular outflows (Shu et al. 1988). This ‘‘X-wind’’ picture was later generalized to account for the stellar accretion and wind generation of T Tauri stars, which have stellar rotational speeds much lower than breakup (Shu et al. 1994). In this case, mass accreting from the inner disk is channeled through a stellar magnetosphere onto the star (Hartmann et al. 1994), while angular momentum is fed back to the disk and out into a strong stellar wind that eventually collimates into a jet (Shu et al. 1995).

Overall, this generalized picture is successful in accounting for many observed properties of T Tauri stars. Study of the younger Class Is finds they similarly exhibit signs of magnetospheric accretion (Doppmann et al. 2005), with evidence for kilo-gauss strength magnetic fields (Johns-Krull et al. 2009). This mounting evidence suggests that Class I protostars can also be magnetically coupled to their accretion disks, although likely at smaller radii than Class II sources (Greene & Lada 2002) given the observed higher rotation rates for Class Is than Class IIs in the same region (Covey et al. 2005). It is yet to be seen, however, whether organized stellar magnetic fields can arise in the earlier Class 0 phase, and subsequently whether they accrete directly from their disks (e.g., via a boundary layer) or via a stellar magnetosphere.

We investigate these open questions with new near-IR spectroscopic observations, which probe the near stellar environment of our Class 0s. This wavelength regime offers three primary spectral features to diagnose potential accretion activity. Br γ emission has been associated with accretion and a signature for magnetospheric activity in Class Is and IIs (Najita et al. 1996b, Muzerolle et al. 1998). CO overtone emission is another strong indicator of active accretion, implying warm ($\geq 2000\text{K}$) temperatures and high ($>10^{10} \text{ cm}^{-3}$) local densities (Geballe & Persson 1987, Carr 1989). High resolution spectroscopy of these features have strongly argued in favor of a Keplerian, rotating disk as the emitting source (Carr et al. 1993, Najita et al. 1996a). Finally, H_2 emission is often interpreted as a signal for strong, bipolar jets or a wind and can offer insight into Class 0 outflow activity.

In this paper, we analyze our observed near-IR spectra of Class 0 protostars using multiple line diagnostics and investigate potential differences to the published results of more evolved Class I and II sources. In Section 2, we describe the target selection criteria used to establish our final Class 0 sample. We also report the source and nature of our data along with our data reduction and processing procedures. In Section 3, we report the

results from the multiple line diagnostics of our near-IR spectra and compare our derived values to that of the literature for Class I and II sources. In Section 4, we interpret our results in the context of emission line excitation mechanisms and the circumstellar environments of Class 0 sources. Finally, in Section 5, we conclude with a brief summary of our findings.

2. SAMPLE AND OBSERVATIONS

2.1. Target Selection

In our efforts to investigate the accretion and jet processes of Class 0 protostars, we compile a sample of the most promising candidates for observation from Earth’s Northern Hemisphere. In particular, we adopt criteria to ensure we have bona fide protostars that likely have yet to accrete the majority of their masses and are bright enough in the near-IR to allow for spectroscopic study. We consider both the Perseus and Orion star-forming regions to maximize the potential for our sample to have numerous candidates capable of spectroscopic study.

Protostellar classes are defined observationally by bolometric temperature (T_{bol}), or the temperature of a blackbody having the same mean frequency as the observed continuum spectrum. To this end, we began with the lists of suspected Class 0 ($T_{\text{bol}} < 70 \text{ K}$) protostars in Perseus (c2d *Spitzer* legacy project, Evans et al. 2009) and Orion (*Herschel* Orion Protostar Survey, Furlan et al. 2016). We required significant *Spitzer* IRAC (Fazio et al. 2004) $3.6\text{--}5.8 \mu\text{m}$ fluxes ($\geq 1 \text{ mJy}$) and inspected mm-interferometer observations (Jørgensen et al. 2009, Maury et al. 2010) when available to verify the existence of massive, extended circumstellar envelopes. For the remaining sources, images from the UKIRT Infrared Deep Sky Survey (UKIDSS, Lawrence et al. 2007) were used to measure positions, integrate K-band fluxes, and estimate source FWHM sizes to assess their observation potential. Ideal candidates had compact spatial extent ($\text{FWHM} \leq 2''$) and were bright enough ($K \sim 15\text{--}16$) to maximize the expected S/N of their observation.

From this sample, we observed seven unique targets (5 in Perseus and 2 in Orion). The object positions, UT dates, and total integration times of our observations are given in Table 1.

2.2. Observations and Data Reduction

We obtained moderate resolution and moderate S/N near-IR K-band spectra of our Class 0 protostars on 2019 Oct 12, 13, and 14 UT with mostly clear skies and $0.6''\text{--}0.7''$ seeing. All observations were made with the Keck I telescope on Maunakea Hawaii, using the MOS-FIRE facility spectrograph (McLean et al. 2010, 2012) in its long-slit mode.

Spectra were acquired with a $1''.5$ (8-pixel) wide slit. We measured a spectroscopic resolving power of $R \equiv \lambda/\delta\lambda = 2,400$ (120 km s^{-1}) for seeing-limited point sources at a wavelength of 2.24 microns. Some of our objects, however, are fairly extended (their observed spatial extents are listed in Table 1), likely reducing our spectroscopic resolving power to $R \sim 1700$ in these cases. The plate scale was $0.1798''/\text{pix}$ along the $46''$ slit length. The order-sorting MOSFIRE K filter was used to record the $\lambda = 2\text{--}2.4 \mu\text{m}$ wavelength range in each exposure.

Data were acquired in AB pairs of 120 s long exposures,

Table 1
Journal of Observations

Object	Region	near-IR R.A. (J2000) (hh mm ss.s)	near-IR Dec. (J2000) (^o [′] [″])	UT Date	Int. Time (minutes)	Spatial Extent ^a ([″])	$v_{systemic}$ ^b (km/s)
Per-emb 26	Per	03 25 38.8	30 44 06.2	2019 Oct 14	24	3.4	5.4
Per-emb 25	Per	03 26 37.4	30 15 28.4	2019 Oct 12	32	0.9	5.8
				2019 Oct 13	34	1	
Per-emb 21	Per	03 29 10.7	31 18 20.6	2019 Oct 14	16		
Per-emb 28	Per	03 43 51.0	32 03 08.1	2019 Oct 14	14	2.7	8.6
Per-emb 8	Per	03 44 44.0	32 01 36.2	2019 Oct 13	26	0.9	11
				2019 Oct 14	20	0.9	
HOPS 32	Ori	05 34 35.4	-05 39 59.0	2019 Oct 12	20	0.7	10
HOPS 44	Ori	05 35 10.6	-05 35 06.3	2019 Oct 13	12		

^aThese extents serve as our extractions widths, corresponding to the spatial width of the individual protostellar continua observed in our 2d spectral images. The low SNRs of our Per-emb 21 and HOPS 44 observations precluded the measurement of their spatial extents.

^bSystem velocities used to shift our continuum-detected Class 0 spectra (Figure 1) into their corresponding systemic rest frames (Section 3.2). For our Perseus sources, we use the derived velocities from the C¹⁸O(2-1) line fitting in Stephens et al. 2019. For HOPS 32, we average similarly derived velocity values for other HOPS protostars in Nagy et al. 2020 as a rough proxy.

with the telescope nodded 10[″] along the slit between integrations. The A0 dwarfs HIP 17971 and HIP 27089 were observed to correct the telluric features in the protostar spectra.

All data were reduced using Pypeit (Prochaska et al. 2020), an open-source Python based data reduction pipeline supporting multiple optical and near-IR spectrographs. In Pypeit, a dome flat exposure is first used to auto-identify and trace the slit edges. Spectra are wavelength calibrated with low-order fits to the OH sky lines present in the science frames. Overall, lower RMS fits were achieved using these lines when compared to fits using the arc spectra of our observed Ne and Ar lamp exposures. Both object and standard images are processed by a cosmic ray masking routine, flat fielded and sky subtracted. Constant extraction widths as a function of wavelength (reported in Table 1) are computed from the flux profile of the individual continua, which do not consider further extended emission. Extracted individual spectra for each pair are then co-added. To remove instrumental and atmospheric features, the co-added object spectra were then divided by the corresponding (co-added) spectra of the A0 dwarf observed at similar airmass. When appropriate, we shifted our protostar spectra slightly in wavelength relative to their telluric spectra to minimize telluric artifacts. We multiplied this result by the ($R = 10000$ intrinsically, binned to the dispersion of our data) PHOENIX (Husser et al. 2013) spectrum of the dwarf stellar model that most closely matched its corresponding standard to achieve our telluric-corrected spectra. Lastly, we flux calibrated our spectra by scaling to the K-band fluxes of the corresponding telluric star.

3. RESULTS

We show our near-infrared spectra in Figure 1. From our sample of seven unique targets, we exclude the spectrum of HOPS 44 from the analysis in the following sections, because of its low signal-to-noise. Its reduced spectrum is shown in Appendix Section B. We also do not detect the continuum of Per-emb 21 and only analyze here its observed H₂ emission lines.

Overall, the three main groups of spectral features seen across our near-IR spectra include CO band, H I Brackett (Br) γ , and H₂ emission, with varying intensity. We do not detect any photospheric absorption features for our sample. In Table 2, we report measured equivalent

widths (EW) for the emission features seen in our sample. All derived strength values presented in Table 2 correspond to emission spatially coincident with each object’s continuum source. Subsequently, these strength values do not account for emission extended spatially past the extracted continuum extents listed in Table 1. For undetected lines, we report 3σ upper limits. In addition to EWs, we compute numerous line diagnostics and compare our values to that of the more evolved Class Is in the following sections.

3.1. CO Overtone Emission

We detect emission bands near 2.3 μm in four of our Class 0 objects (Per-emb 25, Per-emb 26, Per-emb 28, and HOPS 32). Their structure is consistent with CO overtone emission. For a direct comparison, we normalize the bands by fitting the shape of the continuum blueward of the first bandhead, with either a linear fit or a low order quadratic, and dividing them by this estimate.

To show that these observed features are consistent with spectrally resolved CO emission, we construct a simple emission model using the family of higher-resolution ($R=10000$) synthetic spectra in the PHOENIX (Husser et al. 2013) library. The spectra of cool M star giants exhibit broad CO absorption features in a low gravity environment similar to a disk atmosphere. With our starting PHOENIX spectra ($T_{\text{eff}} = 3500$ K, $\log g = 1.5$, $[\text{Fe}/\text{H}] = 0$), we apply the following steps to compare to our data.

The synthetic spectrum is first binned down to match the lower spectral resolution of our data. To invert its CO absorption features into emission, we multiply this spectrum by -1 and then fit its continuum as described for our science objects. We divide the corresponding spectrum by this fit and then add back 2 stellar continua (setting the baseline to +1). We also allow for an extra scaling factor, equivalent to the potential contribution of veiling, to improve our matches to the individual band amplitudes. The inverted synthetic spectra are then broadened with a Gaussian filter to match the broader width of each protostar. We manually iterate the width of our Gaussian filter and repeat this process with different PHOENIX model temperatures to achieve the best fit to our data visually (final widths and temperatures shown in Figure 2).

The reasonable match between the continuum-normalized CO bands in our Class 0s and their cor-

responding model spectra (Figure 2) demonstrate that spectrally broadened CO emission is detected. For our observed $v=2-0$ CO bands, we estimate their velocity width by converting our derived sigma of the Gaussian filter to full width half maxes (FWHMs). We report FWHMs ranging from 200 to 350 km s^{-1} (Table 3). From our iterative process, we estimate reasonable visual fits allow for a range of ± 0.5 sigma units around the best fit sigma value, corresponding to an overall FWHM uncertainty of $\sim 50 \text{ km s}^{-1}$ (except in the case of Per-emb 26, which is much less constrained due to the much lower S/N observation).

We find our observed profiles (black, Figure 2) are consistent with those observed in more evolved Class Is and energetic Class IIs (Carr et al. 1993, Najita et al. 1996a, Contreras Peña et al. 2017). In these older sources, the emission is well explained as arising from the heated atmosphere of the inner disk (Calvet et al. 1991). Our measured FWHMs are also similar to other previously observed Class I and IIs (Chandler et al. 1993), which have appeared broadened past 100 km s^{-1} . Given the moderate spectral resolution of our data, however, we are unable to constrain other disk properties (i_{disk} , $v \sin i$) through a detailed model analysis beyond this estimate.

3.2. Brackett γ Equivalent Widths and Line Profiles

We detect Br γ emission in four of our Class 0 objects (Per-emb 8, Per-emb 25, Per-emb 28, and HOPS 32). We begin by comparing our measured Br γ EWs to that of known Class Is. Figure 3 plots the measured EWs of the Br γ line and the CO band at $2.293 \mu\text{m}$ for our sources and the Class Is observed in Connelley & Greene 2010. Overall, we find the broad distribution of the observed Br γ and CO $v=2-0$ band EWs from these Class Is overlaps with that of our Class 0s. This result implies their near-stellar environments, with accretion and the inner disk sensitively traced by our detected Br γ and CO, appear to be similar between Class 0 and Is.

To examine our observed Br γ line profiles, we first shift them into their systemic rest frame. For our Perseus sources, we use the derived velocities from the $\text{C}^{18}\text{O}(2-1)$ line fitting in Stephens et al. 2019, which primarily traces the envelopes surrounding our protostars. Although this analysis has not been conducted for HOPS 32, we refer to the similarly derived velocity values for other HOPS protostars in Nagy et al. 2020 and use their average as a rough proxy. Collectively, these shifts are small in magnitude (on the order of $\sim 10 \text{ km s}^{-1}$). For a proper comparison, we then normalize our profiles by deriving a linear fit to the continuum redward and blueward of the Br γ emission and dividing the spectrum by this estimate. Using the plot routine in IRAF, we fit each Br γ feature with a Gaussian profile to estimate its width. We report the FWHM of the best fit Gaussian in Table 3. All reported FWHMs in Table 3 have had our instrumental velocity resolution of 120 km s^{-1} subtracted out in quadrature. We compare these resultant profiles with that of observed Class Is (Doppmann et al. 2005) in Figure 4. Overall, we find the Class 0 line shapes to be very similar to that of the Class Is and Class IIs, exhibiting a centrally peaked core (FWHM $\sim 200 \text{ km s}^{-1}$) with broad wings extending to $\pm 300 \text{ km s}^{-1}$. These widths are similar to that found for both T Tauri (Folha & Emerson

2001, Najita et al. 1996b) and Class I (Doppmann et al. 2005) sources, roughly $100\text{--}300 \text{ km s}^{-1}$. We discuss the interpretation of our observed profile structure in Section 4.1.

3.3. H_2 Equivalent Widths and Emission Line Ratios

We detect H_2 emission lines in six of our Class 0 objects (Per-emb 8, Per-emb 21, Per-emb 25, Per-emb 26, Per-emb 28, and HOPS 32). Among the numerous H_2 lines observed, we find the $2.1218 \mu\text{m}$ $\text{H}_2 v=1-0 \text{ S}(1)$ emission line is strongest across our sample. Similar to our comparison in Section 3.2, we plot the measured EWs of the Br γ and $\text{H}_2 v=1-0 \text{ S}(1)$ line between our Class 0s and the Class Is from Connelley & Greene 2010 in Figure 5. We find the lack of an obvious correlation between these quantities unsurprising, given the different suspected locations of their emission source. The detected H_2 emission likely originates further out in the outflow regions of the system relative to the detected Br γ and CO emission, which likely originates near the stellar surface.

Three of our Class 0s (HOPS 32, Per-emb 8, and Per-emb 26) show significantly larger H_2 EWs than any of the Class Is from Connelley & Greene 2010. To quantify the magnitude of this difference, we compute the mean H_2 EW between both samples and find they differ by more than the combined standard deviation within each group. We also perform a two-dimensional two-sided KS test between the two samples and find the difference to be statistically significant, reporting a p-value of 0.007.

We note the spectra of our Class 0s do not show any evidence of photospheric absorption features (Figure 1), likely reflective of high veiling in these objects. Comparably, only $\sim 60\%$ of the Class Is that exhibit both H_2 and Br γ in emission were found to be highly veiled. The observed Class Is with low veiling do not appear to exhibit significantly higher H_2 EWs. Given this, we may be seeing evidence of higher Class 0 H_2 flux relative to their photospheric continua in our three outlying Class 0s relative to these observed Class Is.

Similar to our Br γ analysis, we fit a Gaussian profile to our observed $\text{H}_2 v=1-0 \text{ S}(1)$ emission lines in IRAF and report their FWHMs in Table 3 after subtracting out our instrumental resolution (120 km s^{-1}) in quadrature. The FWHMs of this unresolved line, however, are also subject to the variable spatial extents of our objects (Table 1) and are broadly overestimated. We note our derived values likely probe different parts of the corresponding H_2 flows depending on the orientation of our objects. We also report the velocity shift of the emission centroid relative to the rest wavelength of the line ($2.1218 \mu\text{m}$), typically finding velocities of $\geq |50| \text{ km s}^{-1}$. Overall, the shifted, broad widths of our observed H_2 emission lines are consistent with collisional excitation in jets or a wind.

The ratios of particular H_2 emission lines have the ability to constrain the source excitation mechanism responsible for this observed circumstellar emission. Gredel & Dalgarno (1995) find the $\text{H}_2 v = 1-0 \text{ S}(1)$ ($2.1218 \mu\text{m}$) to $v = 2-1 \text{ S}(1)$ line ($2.2477 \mu\text{m}$) ratio is relatively sensitive for differentiating between different excitation mechanisms and calculate predictions for UV excitation, shock-heated gas in the form of a wind, and X-ray excitation of low ionization H_2 . To de-redden our line ratio, we derive rough estimates of the foreground extinction by fitting

the spectral energy distributions (SEDs) of our Class 0 protostars. Our methodology is detailed in Appendix Section A. We note this correction is generally minimal, given the small difference in wavelength between these individual H₂ lines.

We report the reddening-corrected line ratios for our Class 0 sample in Table 3. Similar to the majority of the Class Is studied in [Greene et al. \(2010\)](#), we find the values of our Class 0s are most consistent with collisional excitation via shocked gas in a wind or X-ray excitation but not UV excitation (Figure 6). The more moderate S/N in the fainter H₂ line transitions precludes our ability to compare this result with other line ratios.

3.4. H₂ Extended Emission

We find HOPS 32, Per-emb 26, and Per-emb 8 (the strongest H₂ EW sources, Figure 5) also exhibit H₂ emission extended from the continuum; an example is shown in Figure 7. Our observations of Per-emb 21, while not sensitive enough to detect the continuum, similarly detect variably extended H₂ emission. Per-emb 25 and Per-emb 28 do not show evidence of any off-axis emission. From our 2d images, we report the measured angular extent of the H₂ 1-0 S(1) line in Table 3. In all cases, we find the emission is far extended spatially ($\geq 5''$, i.e., ~ 1250 AU across for our Perseus sources, and $8''$, i.e., ~ 3200 AU for HOPS 32).

We reference the literature for known outflows corresponding to our Class 0 sources in an attempt to find other potential tracers of our extended emission. Numerous Perseus protostars have had their outflow features identified via both sensitive molecular line emission tracing ([Lee et al. 2016](#), [Stephens et al. 2017](#), [Tobin et al. 2018](#)) and H₂ 2.122- μ m imaging surveys ([Davis et al. 2008](#)). In Table 4, we compare published outflow position angles (PAs) with the slit PAs from our observations when possible.

We find that, as expected, extended emission is present when the slit PA is aligned with the PA of a known CO outflow. As an example, Per-emb 8 was observed in [Tobin et al. \(2018\)](#), which found evidence for strong, rotational CO 2-1 emission northwest of the system at a PA of 313° lacking a southeast component. We find this asymmetry reflected in our data given the close alignment with our slit PA, showing the extended H₂ emission spatially offaxis from the continuum in only one direction (Figure 7). Alternatively, the observed H₂ outflow feature identified for Per-emb 25 ([Davis et al. 2008](#)) has a PA close to orthogonal with our slit PA. In this case, its lack of extended H₂ emission is not surprising.

3.5. Line Luminosities

To compute individual line luminosities, we deredden our measured line fluxes using our derived foreground extinction values (Table 3, Appendix A). We note these values are estimates with high uncertainty given the complicated physical nature of our Class 0s (e.g., non-symmetrical envelopes, scattered light). Subsequently, it is difficult to draw robust conclusions from our derived line luminosities. Despite these limitations, we tentatively compare these values with that observed in more evolved systems as a first look between Class 0s and Is.

In Figure 8, we compare our derived, dereddened H₂ v=1-0 S(1) line luminosity with that of the Class Is from

[Connelley & Greene 2010](#). We find our Class 0s appear to exhibit a wider range of H₂ v=1-0 S(1) line luminosities than Class Is, with a roughly similar median value between both samples (vertical red and black dashed lines, left). Given our foreground extinction estimates are likely lower limits to the true extinction, we consider the effect on this comparison after increasing our extinction estimates to a potentially more appropriate value. We consider the highly accreting Class I protostars in Rho Ophiuchi as a rough proxy, which have continuum brightness of $K \sim 10$ mag with estimated A_v of ~ 20 mag. An overall foreground extinction estimate of $A_v \sim 50$ magnitudes would be consistent with our Class 0 continuum brightnesses of $K \sim 15$ -16 mag after scaling to the distance of Perseus. While the true extinctions to our Class 0 sources could be larger than this estimate, it is unlikely to be considerably so (i.e., $A_v \geq 100$) given that we detect emission from the near-stellar region and our near-IR flux is likely dominated by scattered light. Although the application of this correction to our median Class 0 H₂ v=1-0 S(1) line luminosity (red dashed line, right) implies a potential difference between these two samples, we emphasize it remains unclear the extent to which these line luminosities between these two populations differ until more precise Class 0 extinction estimates can be derived.

We also compare our Br γ luminosities with that of observed YSOs, referencing low mass Class I and IIs from the literature. In Figure 9, we show their respective luminosity distributions. Similar to Figure 8, we show the derived Br γ line luminosity median for our Class 0s using the foreground extinction estimates from our SED fitting (vertical red dashed line, left) and a corrected extinction value of 50 mag for all of our Class 0 sources (vertical red dashed line, right). With an $A_v=50$, the median Class 0, I, and II Br γ luminosities are similar. More precise Class 0 extinction estimates are needed to make a reliable quantitative comparison.

We note our high extinction uncertainties also preclude our ability to derive robust mass accretion rate estimates from our Br γ luminosities, as has been done for Class Is and IIs ([Muzerolle et al. 1998](#), [Fiorellino et al. 2021](#)).

4. DISCUSSION

The line diagnostics analyzed in Section 3 probe the near-circumstellar environment of our Class 0 sample and lend insight into the accretion and outflow processes underway in these YSOs. Here, we compare our measured Class 0 properties with those of well-studied Class I and II sources to investigate the nature of the near-circumstellar environment at the earliest observable stage of evolution.

4.1. Class 0 Stellar Magnetospheres

In Section 3.2, we find our Class 0 sample has broad, centrally peaked (Figure 4) Br γ line profiles (FWHM ~ 200 km s⁻¹) with wings extending to high velocity (300 km s⁻¹). Similar profiles are observed in many Class II ([Najita et al. 1996b](#), [Folha & Emerson 2001](#)) and Class I ([Doppmann et al. 2005](#), [Connelley & Greene 2010](#)) sources. In these more evolved sources, the Br γ profiles are often considered strong evidence for magnetospheric accretion, in which the inner region of the hot

circumstellar disk is channeled by stellar magnetic field lines onto the surface of the star at high infall velocities.

Models of emission from magnetospheric accretion in the Balmer lines (Calvet & Hartmann 1992, Romanova et al. 2012) and Br γ (Muzerolle et al. 1998) have had success reproducing these observed profile shapes. This interpretation is supported by measurements of strong (approaching 3 kG) stellar magnetic fields in Class II (Johns-Krull 2007) and Class I (Johns-Krull et al. 2009) sources.

While Class 0 magnetic field strengths have yet to be estimated directly, the similarity between our Class 0 Br γ profiles and those of these more evolved sources argues in favor of a shared accretion mechanism. These results provide evidence of protostellar magnetic fields and magnetospheres being established very early in the star formation process, at the earliest times yet probed.

4.2. Comparison of Class 0 and Class I/II Accretion Activity

Although our Class 0 sample is small, we note the high frequency of our detected spectral features in emission. There have been few other Class 0s that have had their near-IR spectroscopic observations analyzed for both emission and absorption components. Serpens S68N also exhibited H₂ emission but was absent in Br γ and showed CO bands in absorption rather than emission (Greene et al. 2018). We report the incidence rates of these features in emission among our 5 continuum-detected Class 0s (Figure 1) and Serpens S68N in Table 5. We compare these rates with those of Class Is in nearby molecular clouds (Doppmann et al. 2005). These Class I statistics are similar to what has also been observed in a larger, all-sky sample of Class I protostars (Connelley & Greene 2010).

We find similarly high rates of Br γ emission between the Class 0 and Class I samples, consistent with the active mass assembly expected at these young ages. For both CO and H₂, however, we find notably higher emission incidence rates for Class 0s relative to Class Is.

The high prevalence of CO emission among our Class 0s suggests differences in the inner accretion disks of these objects relative to that of Class Is. Our observations find that the atmospheres of Class 0 inner disks frequently achieve the warm (≥ 2000 K), dense environments ($> 10^{10}$ cm⁻³) required for CO emission, strongly suggestive of a higher average disk accretion rate for Class 0s than Class Is. We perform a Fischer’s exact test and find this result is statistically significant, with a nominal p-value of 0.01. A high accretion rate for Class 0 sources is consistent with the low incidence rate of photospheric absorption features among Class 0s relative to Class Is. Currently, absorption features (Na I and Ca I, 2.21 and 2.26 μ m respectively) have only been observed in Serpens S68N, where it is detected weakly. The low incidence rate is likely a consequence of higher veiling in Class 0s produced by strong continuum emission from their inner warm disks.

The high disk accretion rate implied by these results (CO emission, high veiling) could be similar to that inferred for active Class Is (Fiorellino et al. 2021) and EXors (Aspin et al. 2010), two groups that have also shown near-IR features in emission and have estimated accretion rates of ($\sim 10^{-7}$ – 10^{-6} M_⊙ yr⁻¹). At a higher

disk accretion rate, more similar to that of FU Ori ($\sim 10^{-4}$ M_⊙ yr⁻¹), the CO overtone bands would appear in absorption (Calvet et al. 1991) and the magnetosphere would be crushed, reducing or eliminating the Br γ emission. At much lower disk accretion rates typical of Class II T Tauri stars ($\sim 10^{-8}$ M_⊙ yr⁻¹), the inner disk would not be warm enough over a large enough vertical column density to produce CO overtone emission.

At a disk accretion rate of $\sim 10^{-6}$ M_⊙ yr⁻¹, a protostar can sustain a stellar magnetosphere (and produce the Br γ line profiles we observe) if it has developed a strong, organized stellar magnetic field. If our Class 0 sources have a protostellar mass of 0.2 M_⊙ (as measured for the similarly low-luminosity Class 0 source L1527 IRS; Tobin et al. 2012) and a stellar surface gravity ($\log g$) of 2.38 (as measured for Serpens S68N; Greene et al. 2018), protostellar radii are ~ 4 – 5 R_⊙. If the Class 0 sources further have a disk accretion of $\sim 10^{-6}$ M_⊙ yr⁻¹ and their stellar magnetospheres truncate the inner disk at ~ 2 stellar radii (as measured for the Class I YLW 15; Greene & Lada 2002), the required protostellar magnetic field strength is ~ 1 kG (Hartmann et al. 2016 and references therein). Thus, the CO overtone emission, strong veiling, and Br γ we observe are all plausibly consistent with Class 0 inner disk accretion rates of $\sim 10^{-6}$ M_⊙ yr⁻¹ and approximately kilogauss strength protostellar magnetic fields.

Even within our small sample, several sources depart from the simple picture described above. Unlike the majority of sources in our Class 0 sample, Per-emb 26 exhibits CO overtone emission but no Br γ emission. This object may be in an intermediate state, with a slightly higher accretion rate than the majority of our Class 0s. An accretion level of this magnitude could plausibly suppress the stellar magnetosphere, explaining the absence of Br γ , while still remaining below an FU Ori accretion level, allowing for CO emission (rather than absorption). As a variant in a different direction, the recent near-IR spectrum of Serpens S68N lacks Br γ emission and exhibited CO bands in absorption (Greene et al. 2018). Serpens S68N is likely in a state of lower disk accretion than our Class 0s, with low veiling indicated by its observed photospheric absorption features (Na I, Ca I). Its modest derived $\log g$ value (2.38) is more consistent with a low-gravity stellar photosphere than a disk. Its inflated radius implied by this derivation may be evidence of a significant, recent accretion episode, depleting the reservoir of available accreting material in its disk.

4.3. Nature of the H₂ Emission

We interpret the results from our multiple line diagnostics in Section 3 to assess the nature of the H₂ emission seen in our Class 0 sample. We find our Class 0 H₂ emission properties are often similar to that of known Class Is but in some cases enhanced, indicating higher EWs (Figure 5) and large spatial extensions (Figure 7).

In our attempt to constrain the most likely H₂ excitation, we derived 1–0 S(1)/2–1 S(1) line ratios that argue in favor of either shock-heated gas or X-ray excitation. If excited by collisions in shocks, the molecular hydrogen ortho:para ratio can also be derived with little sensitivity to the H₂ rotation temperature from the $v=1-0$ S(1) and $v=1-0$ S(0) line ratio (Kristensen et al. 2007). From their equation 5, we find ortho:para ratios

ranging from 2.3–2.9 assuming a rotational temperature of 3500 K across our sample. This result provides further evidence of molecular hydrogen emission in shocks as Wilgenbus et al. (2000) finds the hydrogen atom exchanges in shocks set the high temperature limit to $o/p \leq 3$.

We query the literature for observations of X-ray activity in our Class 0 sample, which may also suggest ongoing accretion. X-ray activity can be quantified via an object’s hardness ratio [HR = $(N_h - N_s)/(N_h + N_s)$], where N_h and N_s are the detected counts in the hard (2–8 keV) and soft (0.5–2 keV) energy bands, respectively. Stassun et al. (2004) computed the extinction-corrected hardness ratios between a sample of non-accreting weakly-lined TTS and accreting classical TTS, finding the latter population was more likely to have high HRs.

Despite the likely high visual extinctions expected towards our Class 0s, we find Per-emb 8 has been detected by *Chandra* measurements (Wang et al. 2016). Following the analysis of Stassun et al. (2004), we correct our derived value for extinction. The corrected HR value for Per-emb 8 (~ 0.3) lies near the very high end of the distribution for PMS stars. We find this result, while not a definitive indicator for accretion, is consistent with our cumulative evidence that our Class 0s are likely undergoing active accretion. In particular, the strong X-ray activity observed in Per-emb 8 could be further evidence of organized magnetic fields being plausibly established by Class 0s, supported by the recent observations of Class 0 HOPS 383 (Grosso et al. 2020).

Collectively, these findings are consistent with the properties expected from a strong jet or wind. The recent observation of an extended jet observed toward Per-emb 8 (Tychoniec et al. 2018) argues in favor of the former interpretation as a potential source for the observed X-ray emission. We note our derived H_2 line ratios are consistent with mechanical excitation (Figure 6), which may be due to the shocked gas expected in a strong protostellar jet. Overall, the observed high velocity, often extended, H_2 emission in this work may be evidence of the driving force behind the molecular outflows commonly observed in Class 0s. Future observations of additional Class 0s will be required to further characterize the predominant inner H_2 emission source at this evolutionary stage.

5. SUMMARY AND CONCLUSION

We present new observations of near-infrared *K*-band spectroscopy for a sample of 7 Class 0 protostars in the Perseus and Orion molecular clouds. The H_2 , Br γ , and CO $v=2-0$ band features we detect probe the inner circumstellar environments of these systems (Figure 1). The lack of observed stellar absorption features indicates high continuum veiling, likely from an inner disk with a high accretion rate.

1. Our Class 0 Br γ line profiles are broad, centrally peaked, and similar in shape to those of previously observed Class Is (Figure 4) and strongly suggestive of magnetospheric accretion. This result suggests that organized stellar magnetic fields are established very early, at the earliest observable stage of their evolution.
2. The high frequency of CO band emission observed

in our Class 0s (4/6 \cong 67%) relative to observed Class Is (8/52 \cong 15%) is strongly suggestive of a higher average disk accretion rate for Class 0s. A disk accretion rate of $\sim 10^{-6} M_\odot \text{ yr}^{-1}$ is consistent with the spectral features we observe in our Class 0 spectra, high enough to produce the conditions for CO overtone emission while not high enough to crush the stellar magnetosphere suggested by our Br γ emission if the protostellar magnetic field is approximately kilogauss in strength.

3. Our H_2 line analysis (Section 3.3) derives line ratios that argue in favor of shocks as their source excitation mechanism, similar to that of observed Class Is. Along with the large H_2 spatial extensions and prevalence of H_2 emission we observe in our Class 0s, we interpret this as evidence of strong jets or a disk wind in the near stellar environment, consistent with earlier evidence for strong outflows in these systems on larger scales.

Taken collectively, these results are beginning to characterize the accretion properties of Class 0s. In particular, we find Class 0 protostars may share more similarities with their Class I counterparts than previously thought, with evidence of inner disk accretion properties similar to actively accreting Class Is and magnetospheres being established at the earliest observable evolutionary stages. These organized magnetic fields appear to be plausibly capable of mediating the accretion process, as Class 0s build towards their final mass.

This research has made use of the SIMBAD database and the VizieR catalogue access tool, operated at CDS, Strasbourg, France. This research has also made use of NASA’s Astrophysics Data System and ds9, a tool for data visualization supported by the Chandra X-ray Science Center (CXC) and the High Energy Astrophysics Science Archive Center (HEASARC) with support from the JWST Mission office at the Space Telescope Science Institute for 3D visualization. Multiple Python libraries aided the analysis of our data including matplotlib, a Python library for publication quality graphics (Hunter 2007), SciPy (Virtanen et al. 2020), NumPy (Harris et al. 2020), and Astropy, a community-developed core Python package for Astronomy (Astropy Collaboration et al. 2018, 2013). IRAF is distributed by the National Optical Astronomy Observatory, which is operated by the Association of Universities for Research in Astronomy (AURA) under cooperative agreement with the National Science Foundation (Tody 1993). These acknowledgements were compiled using the Astronomy Acknowledgement Generator.

The authors also wish to recognize and acknowledge the very significant cultural role and reverence that the summit of Mauna Kea has always had within the indigenous Hawaiian community. We are most fortunate to have the opportunity to conduct observations from this mountain. This work was supported by a NASA Keck PI Data Award, administered by the NASA Exoplanet Science Institute. Data presented herein were obtained at the W. M. Keck Observatory from telescope time allocated to the National Aeronautics and Space Administration through the agency’s scientific partnership with

the California Institute of Technology and the University of California. The Observatory was made possible by the generous financial support of the W.M. Keck Foundation.

REFERENCES

- Andre, P., Ward-Thompson, D., & Barsony, M. 1993, *ApJ*, 406, 122, doi: [10.1086/172425](https://doi.org/10.1086/172425)
- Antonucci, S., Nisini, B., Giannini, T., & Lorenzetti, D. 2008, *A&A*, 479, 503, doi: [10.1051/0004-6361:20077468](https://doi.org/10.1051/0004-6361:20077468)
- Arce, H. G., & Goodman, A. A. 2001, *ApJ*, 554, 132, doi: [10.1086/321334](https://doi.org/10.1086/321334)
- Aso, Y., Ohashi, N., Aikawa, Y., et al. 2017, *ApJ*, 849, 56, doi: [10.3847/1538-4357/aa8264](https://doi.org/10.3847/1538-4357/aa8264)
- Aspin, C., Reipurth, B., Herczeg, G. J., & Capak, P. 2010, *ApJL*, 719, L50, doi: [10.1088/2041-8205/719/1/L50](https://doi.org/10.1088/2041-8205/719/1/L50)
- Astropy Collaboration, Robitaille, T. P., Tollerud, E. J., et al. 2013, *A&A*, 558, A33, doi: [10.1051/0004-6361/201322068](https://doi.org/10.1051/0004-6361/201322068)
- Astropy Collaboration, Price-Whelan, A. M., Sipőcz, B. M., et al. 2018, *AJ*, 156, 123, doi: [10.3847/1538-3881/aabc4f](https://doi.org/10.3847/1538-3881/aabc4f)
- Calvet, N., & Hartmann, L. 1992, *ApJ*, 386, 239, doi: [10.1086/171010](https://doi.org/10.1086/171010)
- Calvet, N., Patino, A., Magris, G. C., & D'Alessio, P. 1991, *ApJ*, 380, 617, doi: [10.1086/170618](https://doi.org/10.1086/170618)
- Carr, J. S. 1989, *ApJ*, 345, 522, doi: [10.1086/167927](https://doi.org/10.1086/167927)
- Carr, J. S., Tokunaga, A. T., Najita, J., Shu, F. H., & Glassgold, A. E. 1993, in *American Astronomical Society Meeting Abstracts*, Vol. 181, American Astronomical Society Meeting Abstracts #181, 116.05
- Chandler, C. J., Carlstrom, J. E., Scoville, N. Z., Dent, W. R. F., & Geballe, T. R. 1993, *ApJL*, 412, L71, doi: [10.1086/186943](https://doi.org/10.1086/186943)
- Connelley, M. S., & Greene, T. P. 2010, *AJ*, 140, 1214, doi: [10.1088/0004-6256/140/5/1214](https://doi.org/10.1088/0004-6256/140/5/1214)
- Contreras Peña, C., Lucas, P. W., Kurtev, R., et al. 2017, *MNRAS*, 465, 3039, doi: [10.1093/mnras/stw2802](https://doi.org/10.1093/mnras/stw2802)
- Covey, K. R., Greene, T. P., Doppmann, G. W., & Lada, C. J. 2005, *AJ*, 129, 2765, doi: [10.1086/429736](https://doi.org/10.1086/429736)
- Davis, C. J., Scholz, P., Lucas, P., Smith, M. D., & Adamson, A. 2008, *MNRAS*, 387, 954, doi: [10.1111/j.1365-2966.2008.13247.x](https://doi.org/10.1111/j.1365-2966.2008.13247.x)
- Doppmann, G. W., Greene, T. P., Covey, K. R., & Lada, C. J. 2005, *AJ*, 130, 1145, doi: [10.1086/431954](https://doi.org/10.1086/431954)
- Dunham, M. M., Stutz, A. M., Allen, L. E., et al. 2014, in *Protostars and Planets VI*, ed. H. Beuther, R. S. Klessen, C. P. Dullemond, & T. Henning, 195, doi: [10.2458/azu_uapress-9780816531240-ch009](https://doi.org/10.2458/azu_uapress-9780816531240-ch009)
- Dunham, M. M., Allen, L. E., Evans, Neal J., I., et al. 2015, *ApJS*, 220, 11, doi: [10.1088/0067-0049/220/1/11](https://doi.org/10.1088/0067-0049/220/1/11)
- Durisen, R. H., Yang, S., Cassen, P., & Stahler, S. W. 1989, *ApJ*, 345, 959, doi: [10.1086/167965](https://doi.org/10.1086/167965)
- Enoch, M. L., Young, K. E., Glenn, J., et al. 2006, *ApJ*, 638, 293, doi: [10.1086/498678](https://doi.org/10.1086/498678)
- Evans, Neal J., I., Dunham, M. M., Jørgensen, J. K., et al. 2009, *ApJS*, 181, 321, doi: [10.1088/0067-0049/181/2/321](https://doi.org/10.1088/0067-0049/181/2/321)
- Fazio, G. G., Hora, J. L., Allen, L. E., et al. 2004, *ApJS*, 154, 10, doi: [10.1086/422843](https://doi.org/10.1086/422843)
- Fiorellino, E., Manara, C. F., Nisini, B., et al. 2021, *arXiv e-prints*, arXiv:2103.03863, <https://arxiv.org/abs/2103.03863>
- Folha, D. F. M., & Emerson, J. P. 2001, *A&A*, 365, 90, doi: [10.1051/0004-6361:20000018](https://doi.org/10.1051/0004-6361:20000018)
- Furlan, E., Fischer, W. J., Ali, B., et al. 2016, *ApJS*, 224, 5, doi: [10.3847/0067-0049/224/1/5](https://doi.org/10.3847/0067-0049/224/1/5)
- Geballe, T. R., & Persson, S. E. 1987, *ApJ*, 312, 297, doi: [10.1086/164873](https://doi.org/10.1086/164873)
- Getman, K. V., Broos, P. S., Kuhn, M. A., et al. 2017, *ApJS*, 229, 28, doi: [10.3847/1538-4365/229/2/28](https://doi.org/10.3847/1538-4365/229/2/28)
- Gredel, R., & Dalgarno, A. 1995, *ApJ*, 446, 852, doi: [10.1086/175843](https://doi.org/10.1086/175843)
- Greene, T. P., Barsony, M., & Weintraub, D. A. 2010, *ApJ*, 725, 1100, doi: [10.1088/0004-637X/725/1/1100](https://doi.org/10.1088/0004-637X/725/1/1100)
- Greene, T. P., Gully-Santiago, M. A., & Barsony, M. 2018, *ApJ*, 862, 85, doi: [10.3847/1538-4357/aacc6c](https://doi.org/10.3847/1538-4357/aacc6c)
- Greene, T. P., & Lada, C. J. 2002, *AJ*, 124, 2185, doi: [10.1086/342861](https://doi.org/10.1086/342861)
- Grosso, N., Hamaguchi, K., Principe, D. A., & Kastner, J. H. 2020, *A&A*, 638, L4, doi: [10.1051/0004-6361/202038185](https://doi.org/10.1051/0004-6361/202038185)
- Harris, C. R., Millman, K. J., van der Walt, S. J., et al. 2020, *Nature*, 585, 357, doi: [10.1038/s41586-020-2649-2](https://doi.org/10.1038/s41586-020-2649-2)
- Harsono, D., Jørgensen, J. K., van Dishoeck, E. F., et al. 2014, *A&A*, 562, A77, doi: [10.1051/0004-6361/201322646](https://doi.org/10.1051/0004-6361/201322646)
- Hartmann, L., Herczeg, G., & Calvet, N. 2016, *ARA&A*, 54, 135, doi: [10.1146/annurev-astro-081915-023347](https://doi.org/10.1146/annurev-astro-081915-023347)
- Hartmann, L., Hewett, R., & Calvet, N. 1994, *ApJ*, 426, 669, doi: [10.1086/174104](https://doi.org/10.1086/174104)
- Houck, J. R., Roellig, T. L., van Cleve, J., et al. 2004, *ApJS*, 154, 18, doi: [10.1086/423134](https://doi.org/10.1086/423134)
- Hunter, J. D. 2007, *Computing In Science & Engineering*, 9, 90
- Husser, T. O., Wende-von Berg, S., Dreizler, S., et al. 2013, *A&A*, 553, A6, doi: [10.1051/0004-6361/201219058](https://doi.org/10.1051/0004-6361/201219058)
- Johns-Krull, C. M. 2007, *ApJ*, 664, 975, doi: [10.1086/519017](https://doi.org/10.1086/519017)
- Johns-Krull, C. M., Greene, T. P., Doppmann, G. W., & Covey, K. R. 2009, *ApJ*, 700, 1440, doi: [10.1088/0004-637X/700/2/1440](https://doi.org/10.1088/0004-637X/700/2/1440)
- Jørgensen, J. K., van Dishoeck, E. F., Visser, R., et al. 2009, *A&A*, 507, 861, doi: [10.1051/0004-6361/200912325](https://doi.org/10.1051/0004-6361/200912325)
- Kim, S.-H., Martin, P. G., & Hendry, P. D. 1994, *ApJ*, 422, 164, doi: [10.1086/173714](https://doi.org/10.1086/173714)
- Kirk, H., Johnstone, D., & Di Francesco, J. 2006, *ApJ*, 646, 1009, doi: [10.1086/503193](https://doi.org/10.1086/503193)
- Kounkel, M., Hartmann, L., Loinard, L., et al. 2017, *ApJ*, 834, 142, doi: [10.3847/1538-4357/834/2/142](https://doi.org/10.3847/1538-4357/834/2/142)
- Kristensen, L. E., Ravkilde, T. L., Field, D., Lemaire, J. L., & Pineau Des Forêts, G. 2007, *A&A*, 469, 561, doi: [10.1051/0004-6361:20065786](https://doi.org/10.1051/0004-6361:20065786)
- Kryukova, E., Megeath, S. T., Gutermuth, R. A., et al. 2012, *AJ*, 144, 31, doi: [10.1088/0004-6256/144/2/31](https://doi.org/10.1088/0004-6256/144/2/31)
- Lawrence, A., Warren, S. J., Almaini, O., et al. 2007, *MNRAS*, 379, 1599, doi: [10.1111/j.1365-2966.2007.12040.x](https://doi.org/10.1111/j.1365-2966.2007.12040.x)
- Lee, K. I., Dunham, M. M., Myers, P. C., et al. 2016, *ApJL*, 820, L2, doi: [10.3847/2041-8205/820/1/L2](https://doi.org/10.3847/2041-8205/820/1/L2)
- Maret, S., Maury, A. J., Belloche, A., et al. 2020, *A&A*, 635, A15, doi: [10.1051/0004-6361/201936798](https://doi.org/10.1051/0004-6361/201936798)
- Maury, A. J., André, P., Hennebelle, P., et al. 2010, *A&A*, 512, A40, doi: [10.1051/0004-6361/200913492](https://doi.org/10.1051/0004-6361/200913492)
- Maury, A. J., André, P., Testi, L., et al. 2019, *A&A*, 621, A76, doi: [10.1051/0004-6361/201833537](https://doi.org/10.1051/0004-6361/201833537)
- McLean, I., Steidel, C., Epps, H., et al. 2012, *Proc. SPIE*, 8446, doi: [10.1117/12.924794](https://doi.org/10.1117/12.924794)
- McLean, I. S., Steidel, C. C., Epps, H., et al. 2010, in *Ground-based and Airborne Instrumentation for Astronomy III*, ed. I. S. McLean, S. K. Ramsay, & H. Takami, Vol. 7735, International Society for Optics and Photonics (SPIE), 568 – 579, doi: [10.1117/12.856715](https://doi.org/10.1117/12.856715)
- Megeath, S. T., Gutermuth, R., Muzerolle, J., et al. 2012, *AJ*, 144, 192, doi: [10.1088/0004-6256/144/6/192](https://doi.org/10.1088/0004-6256/144/6/192)
- Murillo, N. M., van Dishoeck, E. F., Tobin, J. J., & Fedele, D. 2016, *A&A*, 592, A56, doi: [10.1051/0004-6361/201628247](https://doi.org/10.1051/0004-6361/201628247)
- Muzerolle, J., Calvet, N., & Hartmann, L. 1998, *ApJ*, 492, 743, doi: [10.1086/305069](https://doi.org/10.1086/305069)
- Nagy, Z., Menechella, A., Megeath, S. T., et al. 2020, *A&A*, 642, A137, doi: [10.1051/0004-6361/201937342](https://doi.org/10.1051/0004-6361/201937342)
- Najita, J., Carr, J. S., Glassgold, A. E., Shu, F. H., & Tokunaga, A. T. 1996a, *ApJ*, 462, 919, doi: [10.1086/177205](https://doi.org/10.1086/177205)
- Najita, J., Carr, J. S., & Tokunaga, A. T. 1996b, *ApJ*, 456, 292, doi: [10.1086/176649](https://doi.org/10.1086/176649)
- Ortiz-León, G. N., Loinard, L., Dzib, S. A., et al. 2018, *ApJ*, 865, 73, doi: [10.3847/1538-4357/aada49](https://doi.org/10.3847/1538-4357/aada49)
- Plunkett, A. L., Arce, H. G., Mardones, D., et al. 2015, *Nature*, 527, 70, doi: [10.1038/nature15702](https://doi.org/10.1038/nature15702)
- Poglitsch, A., Waelkens, C., Geis, N., et al. 2010, *A&A*, 518, L2, doi: [10.1051/0004-6361/201014535](https://doi.org/10.1051/0004-6361/201014535)
- Prochaska, J. X., Hennawi, J. F., Westfall, K. B., et al. 2020, *arXiv e-prints*, arXiv:2005.06505, <https://arxiv.org/abs/2005.06505>
- Rebull, L. M. 2015, *AJ*, 150, 17, doi: [10.1088/0004-6256/150/1/17](https://doi.org/10.1088/0004-6256/150/1/17)
- Reynolds, N. K., Tobin, J. J., Sheehan, P., et al. 2021, *ApJL*, 907, L10, doi: [10.3847/2041-8213/abcc02](https://doi.org/10.3847/2041-8213/abcc02)
- Rieke, G. H., Young, E. T., Engelbracht, C. W., et al. 2004, *ApJS*, 154, 25, doi: [10.1086/422717](https://doi.org/10.1086/422717)

- Robitaille, T. P., Whitney, B. A., Indebetouw, R., & Wood, K. 2007, *ApJS*, 169, 328, doi: [10.1086/512039](https://doi.org/10.1086/512039)
- Robitaille, T. P., Whitney, B. A., Indebetouw, R., Wood, K., & Denzmore, P. 2006, *ApJS*, 167, 256, doi: [10.1086/508424](https://doi.org/10.1086/508424)
- Romanova, M. M., Ustyugova, G. V., Koldoba, A. V., & Lovelace, R. V. E. 2012, *MNRAS*, 421, 63, doi: [10.1111/j.1365-2966.2011.20055.x](https://doi.org/10.1111/j.1365-2966.2011.20055.x)
- Sandell, G., & Knee, L. B. G. 2001, *ApJL*, 546, L49, doi: [10.1086/318060](https://doi.org/10.1086/318060)
- Segura-Cox, D. M., Looney, L. W., Tobin, J. J., et al. 2018, *ApJ*, 866, 161, doi: [10.3847/1538-4357/aaddf3](https://doi.org/10.3847/1538-4357/aaddf3)
- Shu, F., Najita, J., Ostriker, E., et al. 1994, *ApJ*, 429, 781, doi: [10.1086/174363](https://doi.org/10.1086/174363)
- Shu, F. H., Lizano, S., Ruden, S. P., & Najita, J. 1988, *ApJL*, 328, L19, doi: [10.1086/185152](https://doi.org/10.1086/185152)
- Shu, F. H., Najita, J., Ostriker, E. C., & Shang, H. 1995, *ApJL*, 455, L155, doi: [10.1086/309838](https://doi.org/10.1086/309838)
- Siringo, G., Kreysa, E., Kovács, A., et al. 2009, *A&A*, 497, 945, doi: [10.1051/0004-6361/200811454](https://doi.org/10.1051/0004-6361/200811454)
- Siringo, G., Kreysa, E., De Breuck, C., et al. 2010, *The Messenger*, 139, 20
- Skrutskie, M. F., Cutri, R. M., Stiening, R., et al. 2006, *AJ*, 131, 1163, doi: [10.1086/498708](https://doi.org/10.1086/498708)
- Stassun, K. G., Ardila, D. R., Barsony, M., Basri, G., & Mathieu, R. D. 2004, *AJ*, 127, 3537, doi: [10.1086/420989](https://doi.org/10.1086/420989)
- Stephens, I. W., Dunham, M. M., Myers, P. C., et al. 2017, *ApJ*, 846, 16, doi: [10.3847/1538-4357/aa8262](https://doi.org/10.3847/1538-4357/aa8262)
- Stephens, I. W., Bourke, T. L., Dunham, M. M., et al. 2019, *ApJS*, 245, 21, doi: [10.3847/1538-4365/ab5181](https://doi.org/10.3847/1538-4365/ab5181)
- Stutz, A. M., Tobin, J. J., Stanke, T., et al. 2013, *ApJ*, 767, 36, doi: [10.1088/0004-637X/767/1/36](https://doi.org/10.1088/0004-637X/767/1/36)
- Tobin, J. J., Hartmann, L., Chiang, H.-F., et al. 2012, *Nature*, 492, 83, doi: [10.1038/nature11610](https://doi.org/10.1038/nature11610)
- Tobin, J. J., Chandler, C. J., Wilner, D. J., et al. 2013, *ApJ*, 779, 93, doi: [10.1088/0004-637X/779/2/93](https://doi.org/10.1088/0004-637X/779/2/93)
- Tobin, J. J., Looney, L. W., Li, Z.-Y., et al. 2018, *ApJ*, 867, 43, doi: [10.3847/1538-4357/aae1f7](https://doi.org/10.3847/1538-4357/aae1f7)
- Tobin, J. J., Sheehan, P. D., Reynolds, N., et al. 2020a, *ApJ*, 905, 162, doi: [10.3847/1538-4357/abc5bf](https://doi.org/10.3847/1538-4357/abc5bf)
- Tobin, J. J., Sheehan, P. D., Megeath, S. T., et al. 2020b, *ApJ*, 890, 130, doi: [10.3847/1538-4357/ab6f64](https://doi.org/10.3847/1538-4357/ab6f64)
- Tody, D. 1993, in *Astronomical Society of the Pacific Conference Series*, Vol. 52, *Astronomical Data Analysis Software and Systems II*, ed. R. J. Hanisch, R. J. V. Brissenden, & J. Barnes, 173
- Tychoniec, L., Tobin, J. J., Karska, A., et al. 2018, *ApJS*, 238, 19, doi: [10.3847/1538-4365/aaceae](https://doi.org/10.3847/1538-4365/aaceae)
- Virtanen, P., Gommers, R., Oliphant, T. E., et al. 2020, *Nature Methods*, 17, 261, doi: <https://doi.org/10.1038/s41592-019-0686-2>
- Wang, S., Liu, J., Qiu, Y., et al. 2016, *ApJS*, 224, 40, doi: [10.3847/0067-0049/224/2/40](https://doi.org/10.3847/0067-0049/224/2/40)
- Wilgenbus, D., Cabrit, S., Pineau des Forêts, G., & Flower, D. R. 2000, *A&A*, 356, 1010
- Yen, H.-W., Koch, P. M., Takakuwa, S., et al. 2017, *ApJ*, 834, 178, doi: [10.3847/1538-4357/834/2/178](https://doi.org/10.3847/1538-4357/834/2/178)
- Zucker, C., Speagle, J. S., Schlafly, E. F., et al. 2020, *A&A*, 633, A51, doi: [10.1051/0004-6361/201936145](https://doi.org/10.1051/0004-6361/201936145)

APPENDIX

APPENDIX SECTION A: SPECTRAL ENERGY DISTRIBUTION FITTING

Motivation

Prominent star-forming regions like the Perseus and Orion complexes have been observed by multiple surveys, recording flux measurements for many young stellar objects (YSOs) over a large range of wavelengths (1–1100 μ m). These measurements constitute the spectral energy distribution (SED) of an object; for Class 0s, the properties of the central source, its circumstellar disk, and its massive envelope contribute to the overall shape of the SED. Fitting this shape with an SED model can constrain numerous properties including the orientation of the disk along with the foreground extinction to the object along our line of sight.

For the central object of a Class 0, this extinction can be significantly high, with A_V reaching up to 70–80 magnitudes. A proper comparison of our emission line fluxes with that of the more evolved Class I and II sources requires them to first be de-reddened. In extreme cases, this can account for a large correction to the overall luminosity of the spectral feature.

However, due to degeneracies between the star, disk, and envelope properties, the shape of the SED is often not unique, with a family of SED models able to fit the observed SED. The situation is further complicated by the asymmetrical nature of most Class 0s, as the observed emission leaks out from holes in the envelope and scatters off the walls of the inner cavity. Given these limitations, we take care to not over-interpret the results, solely focused on deriving a rough estimate of the foreground extinction. This estimate is only used to very approximately de-redden our observed line luminosities as a first look comparison with that observed in Class Is (Figure 8 and 9). We note our extinction estimates are likely lower limits, given they do not quantify the envelope’s (likely significant) contribution to the overall extinction. In turn, our estimated Class 0 line luminosities are likely systematically under-estimated and should be considered with care in future work.

Procedure

When constructing our SEDs, we find our Class 0s have varied sampling at both near-IR and mid/far-IR wavelengths. In the near-infrared, we used J , H , and K_s from the Two Micron All Sky Survey (2MASS; [Skrutskie et al. 2006](#)) when available, otherwise supplementing with JHK measurements from UKIDSS ([Lawrence et al. 2007](#)) when possible. In the mid-infrared, the Infrared Array Camera (IRAC; [Fazio et al. 2004](#)) and the Multiband Imaging Photometer (MIPS; [Rieke et al. 2004](#)) on *Spitzer* provided 3.6, 4.5, 5.8, and 8.0 μ m and 24 μ m photometry, respectively. We consider the reported values of this *Spitzer* data from numerous sources and followup observations including [Kryukova et al. 2012](#), [Megeath et al. 2012](#), [Rebull 2015](#), [Dunham et al. 2015](#), and [Getman et al. 2017](#).

When possible, we also use data from the Infrared Spectrograph (IRS; [Houck et al. 2004](#)) on *Spitzer*. HOPS 32, Per-emb 21, 25, and 28 were observed by both the Short-Low (SL; 5.2–14 μ m) and Long-Low (LL; 14–38 μ m) modules whereas Per-emb 26 was only observed in SL. In the far-infrared, some of our Perseus sources have recorded 70, 100, and 160 μ m fluxes (derived from *Herschel* PACS maps in [Murillo et al. 2016](#)) and, in some cases, *Spitzer* MIPS 70 μ m

fluxes. We consider both datasets in our attempt to improve the sampling of the SED peaks. HOPS 32 has recorded Herschel PACS (Poglitsch et al. 2010) data at 70, 100, and 160 μm .

Similarly, some of our Perseus sources also have 450, 850 μm SCUBA (Sandell & Knee 2001, Kirk et al. 2006) and 1.1 mm Bolocam (Enoch et al. 2006) measurements while HOPS 32 has 350 and 870 μm (Stutz et al. 2013) by the APEX telescope using the LABOCA and SABOCA instruments (Siringo et al. 2009, 2010, respectively).

To fit the observed SEDs, we use the YSO SED models of Robitaille et al. 2006, which consists of a pre-computed grid of 200,000 total models. Overall, our approach adopts the recommendations laid out by Robitaille et al. 2007. In cases where several measurements were available at similar wavelengths, we only used the highest quality one (i.e. MIPS data was favored over lower-resolution IRAS measurements to avoid confusion).

At a given wavelength, many of our sources have been observed in multiple epochs. In some cases, recorded fluxes (particularly in the *Spitzer* IRAC channels but also 2MASS K-band and MIPS 24 μm) show significant variability, up to an order of magnitude for Per-emb 26. In these instances, we average the highest and lowest recorded flux measurements, inflating the error bars to capture the observed range of values. When applicable, this procedure grants the SED fitter more freedom to fit a variety of models for these sources with well-documented activity.

For IRAS, far-infrared, submillimeter, and Bolocam data, a lower limit of 25% was imposed on the flux uncertainties to account for uncertainties in their absolute calibration. For all other measurements without evidence of variability, flux uncertainties were increased to 10% if the recorded uncertainties were smaller.

In some cases, we find discrepancies between the flux measurements recorded at similar wavelengths but by different instruments (the overlap between IRAC channels 3 and 4 and MIPS 24 μm with our IRS spectra). This could be explained by calibration or extraction problems in the IRS spectrum (extended emission around the target or a close companion), or variability. Following the methodology in Furlan et al. 2016, we assumed the former scenario if the flux deviations between IRS and IRAC and between IRS and MIPS were similar and more than 10%, scaling the IRS spectrum to the MIPS 24 μm flux in those cases. We scale the IRS spectrum of Per-emb 25, Per-emb 28, and HOPS 32 by 0.816, 0.548, and 0.648, respectively. Similar to Furlan et al. 2016, we also bin the IRS spectrum to 3 wavelengths after smoothing over its noisy regions to ensure it does not dominate over the photometry. Incorporating the IRS spectra at these wavelengths characterizes the 10 μm silicate feature and the mid-IR slope of the SED, which crucially constrains the resultant fits. Overall, the SEDs tend to have greater coverage at shorter wavelengths, and are thus expected to reproduce the near and mid-IR fluxes better than the sub-millimeter.

Assumed apertures sizes for the various photometry are similar to those used in Robitaille et al. 2007 (2'' for UKIDSS, 3'' for 2MASS, 5'' for IRAC channels, 3.6'' and 10.5'' for IRS in SL mode and LL mode respectively, 10'' for MIPS 24 μm , 20'' for MIPS 70 μm , and 40'' for SCUBA and Bolocam data). Aperture sizes of 9.6'' for PACS 70 μm , 7.2'' for PACS 100 μm , and 12.8'' for PACS 160 μm were used, given the analysis of Murillo et al. 2016.

Given the estimated distance of 300 parsecs to the Perseus molecular cloud (Ortiz-León et al. 2018, Zucker et al. 2020), we adopt a distance search range of 300–340 parsecs for our Perseus sources and a search range of 420–460 parsecs ($d \sim 420$ pc for the Orion Molecular Cloud, Kounkel et al. 2017) for HOPS 32. This range accounts for potential differences in cloud depth for our embedded sources. We adopt an A_V extinction range of 0–100 magnitudes, assuming the extinction law of Kim et al. 1994.

Interpretation of Best-fit Models

In Figure 10, we show the final results from the SED model fitting for our Class 0s. We show the best-fit model in black and the family of models for which $\chi^2 - \chi_{best}^2$ per data point < 3 in grey.

For the majority of our sources, we find the overall family of SED models to be well constrained and small in number. In these cases, the derived foreground extinction values have little variation, deviating by at most only a few magnitudes. In the case of Per-emb 26, however, the significant variability in the IRAC channels and MIPS 24 μm allows for a much larger number of reasonable fits along with a subsequent poor constraint on its foreground visual extinction (ranging ~ 40 magnitudes).

Collectively, we note the best-fit models 1. capture our shortest wavelength points (those most sensitive to extinction and in the regime of the observations presented in this work) and 2. capture the depth of the crucial 10 μm silicate feature well (with the available IRS data for which only Per-emb 8 is lacking). In Table 3, we report our best-fit estimates for the visual foreground extinction to each source, noting the greater uncertainty in the case of Per-emb 26. We report additional parameters output by the SED fitting procedure in Table 6.

APPENDIX SECTION B: HOPS 44 SPECTRUM

Due to the low signal to noise in its spectrum, we choose to exclude HOPS 44 (the faintest object in our sample, $K \sim 16.5$) from the final sample of Class 0 we analyze in Section 3. Interestingly, we may be seeing evidence of photospheric absorption features in its spectrum. We show its reduced (and smoothed) spectrum in Figure 11 and encourage follow-up observations of this promising source.

Table 2
Emission Line Equivalent Widths

Source	1-0 S(2)		2-1 S(3)		1-0 S(1)		2-1 S(2)		3-2 S(3)		1-0 S(0)		2-1 S(1)		Br γ		CO (2-0)		CO (3-1)		CO (4-2)	
	EW (Å)		EW (Å)		EW (Å)		EW (Å)		EW (Å)		EW (Å)		EW (Å)		EW (Å)		EW (Å)		EW (Å)		EW (Å)	
Per-emb 26	57.3 ± 1.1		29.4 ± 1.0		110.0 ± 1.0		8.3 ± 1.0		5.5 ± 1.0		52.4 ± 1.1		16.6 ± 1.1		≤1.3 ^a		25.5 ± 1.6		29.6 ± 1.6		27.6 ± 1.6	
Per-emb 25	2.1 ± 0.2		1.9 ± 0.2		1.7 ± 0.2		0.9 ± 0.2		≤0.2 ^a		3.3 ± 0.2		≤0.2 ^a		4.5 ± 0.3		25.1 ± 0.3		20.3 ± 0.3		19.2 ± 0.3	
Per-emb 28	3.9 ± 0.1		2.0 ± 0.1		6.8 ± 0.1		1.1 ± 0.1		≤0.1 ^a		1.4 ± 0.1		0.8 ± 0.1		2.9 ± 0.1		12.3 ± 0.1		8.6 ± 0.1		≤0.1 ^a	
Per-emb 8	51.0 ± 0.3		9.5 ± 0.3		114.1 ± 0.3		5.7 ± 0.3		2.9 ± 0.4		35.0 ± 0.3		6.3 ± 0.4		6.9 ± 0.4		≤0.5 ^a		≤0.5 ^a		≤0.5 ^a	
HOPS 32	55.4 ± 0.3		14.1 ± 0.3		149.8 ± 0.3		6.2 ± 0.3		3.2 ± 0.3		25.5 ± 0.3		12.5 ± 0.3		4.5 ± 0.4		25.9 ± 0.4		17.5 ± 0.4		11.0 ± 0.4	

All EWs correspond to emission features. We report their absolute values in this table. These EWs do not account for emission extended from the continuum.

^aWe report a 3σ upper limit for this undetected emission line.

Table 3
Emission Line Derivations

Source	CO (2-0) FWHM ^{a, b} km/s	Br γ FWHM ^a km/s	1-0 S(1) FWHM ^{a, c} km/s	1-0 S(1) Offset km/s	1-0 S(1)/2-1 S(1)	1-0 S(1) extent ($''$)	$A_{v,v}$ ^e mag
Per-emb 26	352		119	68	9.4	13	18.7 ^d
Per-emb 25	201	307	129	58			9.3
Per-emb 21			26	-46	19.6	10	36.4
Per-emb 28	202	244	42	75	12.5		4.7
Per-emb 8		219	139	68	11.3	5	20.9
HOPS 32	239	237	50	-15	9.4	8	23.9

^aThe intrinsic instrumental line width of 120 km s^{-1} has been removed in quadrature.

^bThese FWHMs are derived via the width of our Gaussian filter in our synthetic spectra comparison (Section 3.1).

^cThese FWHMs are subject to the variable spatial extents of our objects (Table 1) and are broadly overestimated. (Section 3.3).

^dPoorly constrained due to significant variability in the IRAC photometry of Per-emb 26 (Appendix Section A.3).

^eBest-fit values from SED model analysis (Appendix Section A). We note these derivations are very approximate, likely lower, estimates given the complicated physical nature of Class 0 SEDs (see Section 3.5, Appendix Section A).

Table 4
Position Angle Comparison

Object	Slit PA	Outflow PA	Reference ^a
Per-emb 26	4	162, 165	1, 2
Per-emb 25, Oct 12/13	0, 0	104, 105	1, 2
Per-emb 21	320	48	3
Per-emb 28	150	112	3
Per-emb 8, Oct 13/14	313, 133	314	4

^aReference IDs: [Stephens et al. \(2017\)](#) (1), [Davis et al. \(2008\)](#) (2), [Lee et al. \(2016\)](#) (3), [Tobin et al. \(2018\)](#) (4).

Table 5
Emission Incidence Statistics

Emission Feature	Class 0s ^a	Class 1s ^b
Br γ	4/6 \cong 67%	34/52 \cong 65%
H ₂	6/6 = 100%	23/52 \cong 44%
CO	4/6 \cong 67%	8/52 \cong 15%

^aThis Class 0 sample constitutes the 5 continuum-detected Class 0s from this work (Per-emb 8, Per-emb 25, Per-emb 26, Per-emb 28, and HOPS 32) and Serpens S68N ([Greene et al. 2018](#)).

^bThis Class 1 sample corresponds to the Class 1s observed in nearby dark clouds ([Doppmann et al. 2005](#)).

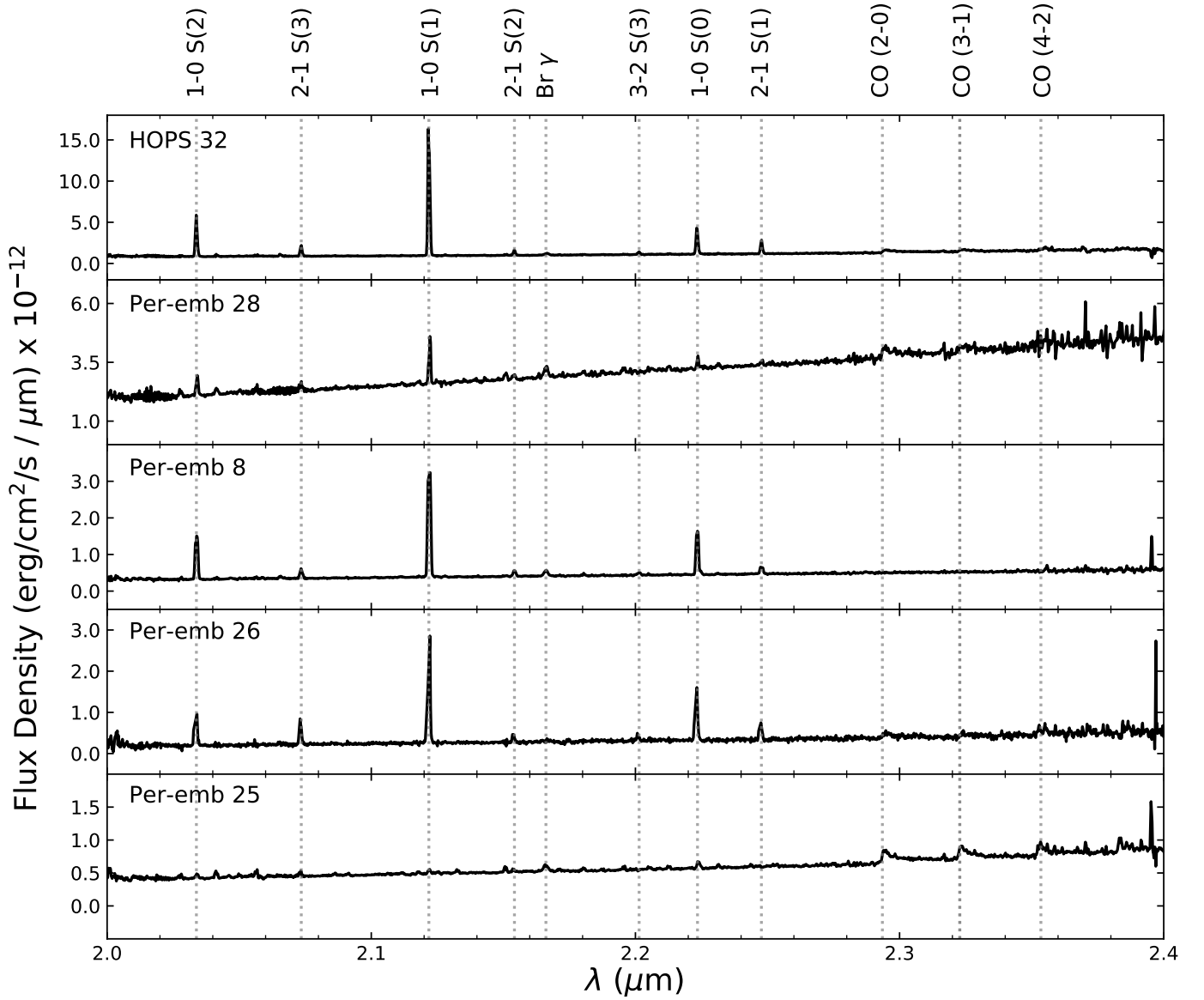


Figure 1. *K*-band spectra of our Class 0 protostar sample, excluding Per-emb 21 and HOPS 44 (see Section 3). We identify the major atomic and molecular emission features present across the spectra (numerous H₂ emission line transitions, Br γ emission, and CO band emission). We refer the reader to Table 2 for a complete census of line feature detection per individual source.

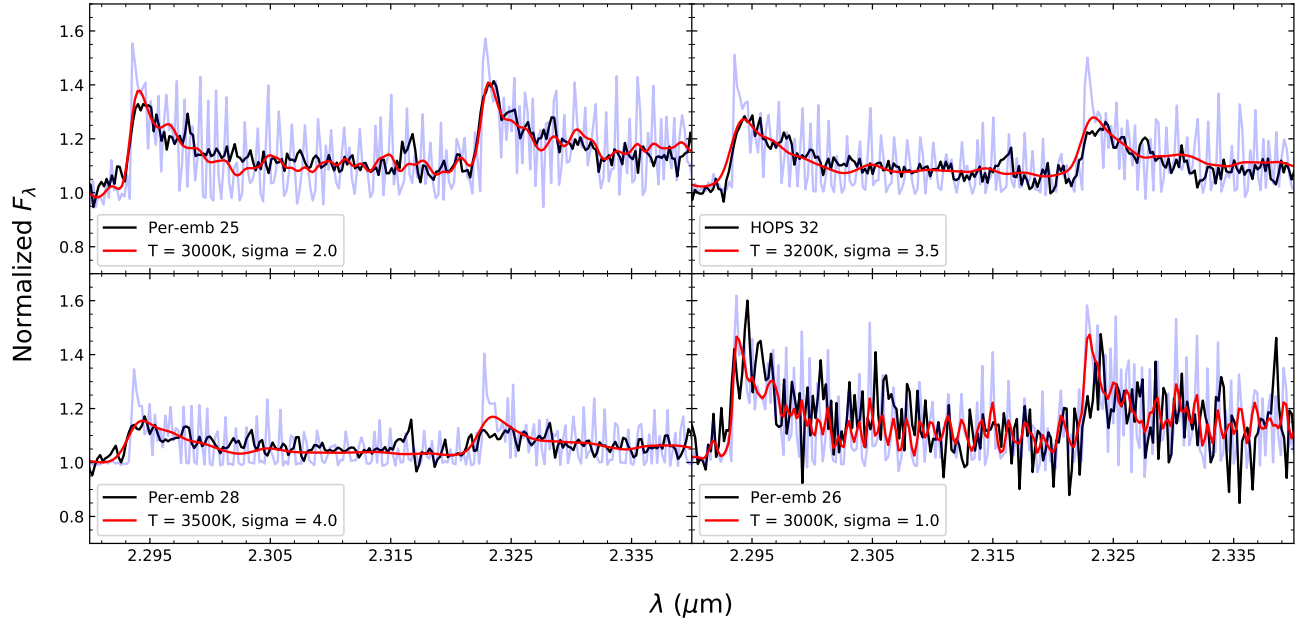


Figure 2. Our observed CO $v=2-0$ emission bands (black) overplotted with that of inverted PHOENIX model spectra before (light blue) and after (red) smoothing with a Gaussian filter (Section 3.1). The reasonable match between our data and model spectra demonstrate that spectrally broadened CO emission is detected in these four Class 0 objects.

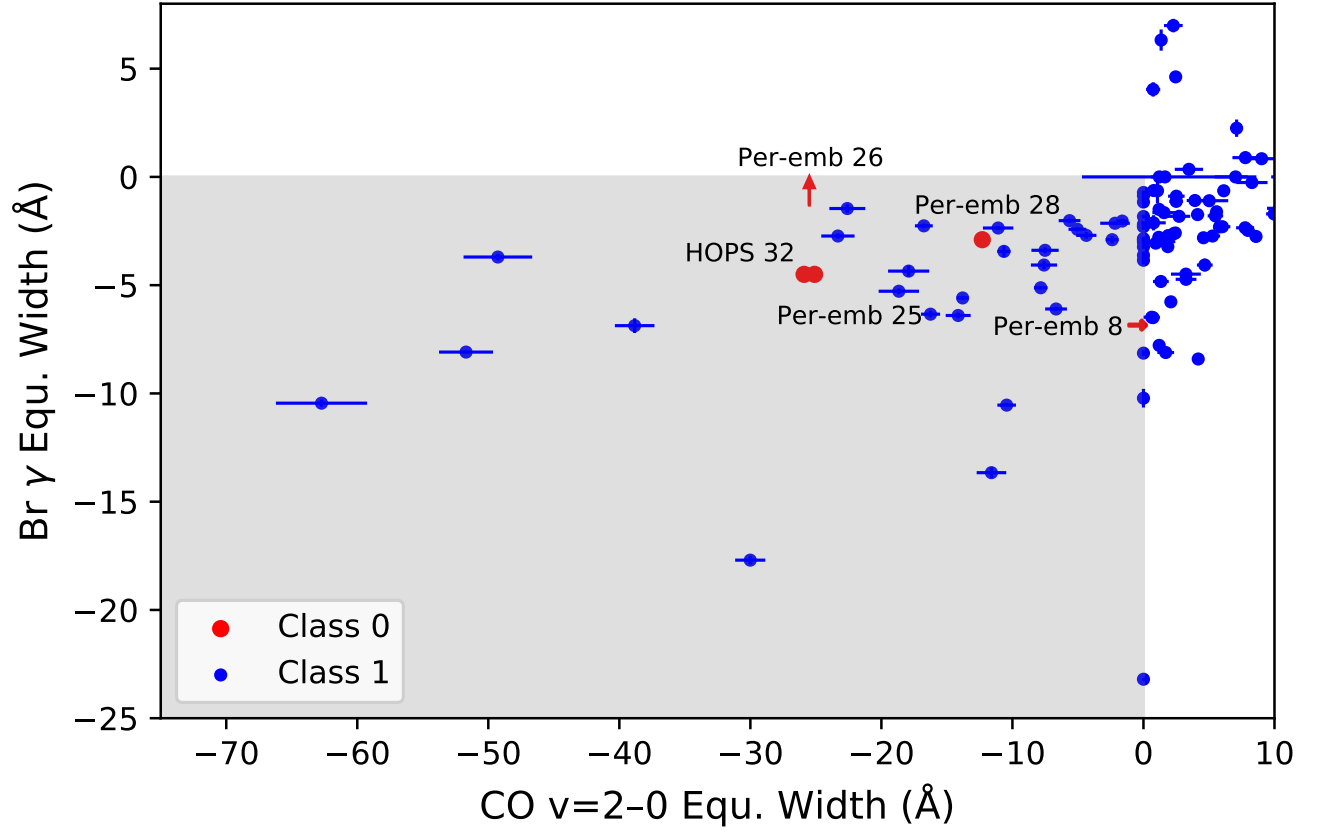


Figure 3. Br γ equivalent widths vs. the CO $v=2-0$ band equivalent widths. Red points correspond to observed Class 0 sources (this work) while blue points correspond to observed Class I sources (Connelley & Greene 2010). The shaded region demarcates sources with observed emission in both features. Undetected lines are represented with arrows, corresponding to 3σ upper limits. We find the broad distribution of these EWs appear to overlap between Class 0 and Is (Section 3.2).

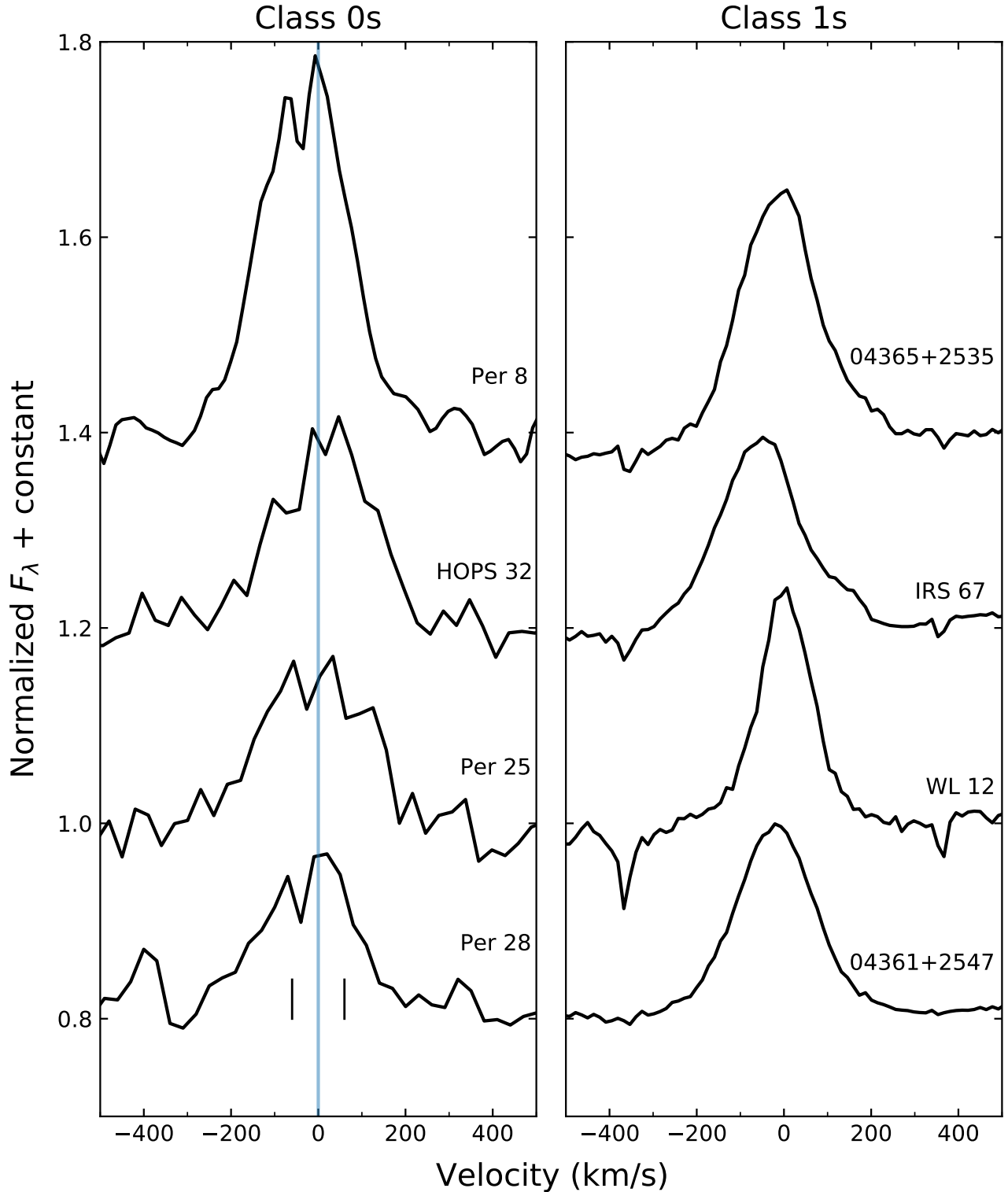


Figure 4. Comparison of observed Br γ line profile between our Class 0s (left) and the Class 1s from [Doppmann et al. \(2005\)](#) (right). Spectra have been normalized with a linear fit to the continuum and shifted into the systemic reference frame (Section 3.2). We overplot a bisecting line in blue to roughly quantify the relative blue and red shifted flux contributions visually. The black ticks represent the approximate velocity resolution of our data (~ 120 km/s). The high resolution spectra of the Class 1s ($R=18,000$) has been downgraded to match our moderate MOSFIRE resolution ($R=2,400$). In Section 4.1, we argue the similarity between our Class 0 line profiles and that of Class 1s hints towards the presence of a magnetosphere at the Class 0 stage.

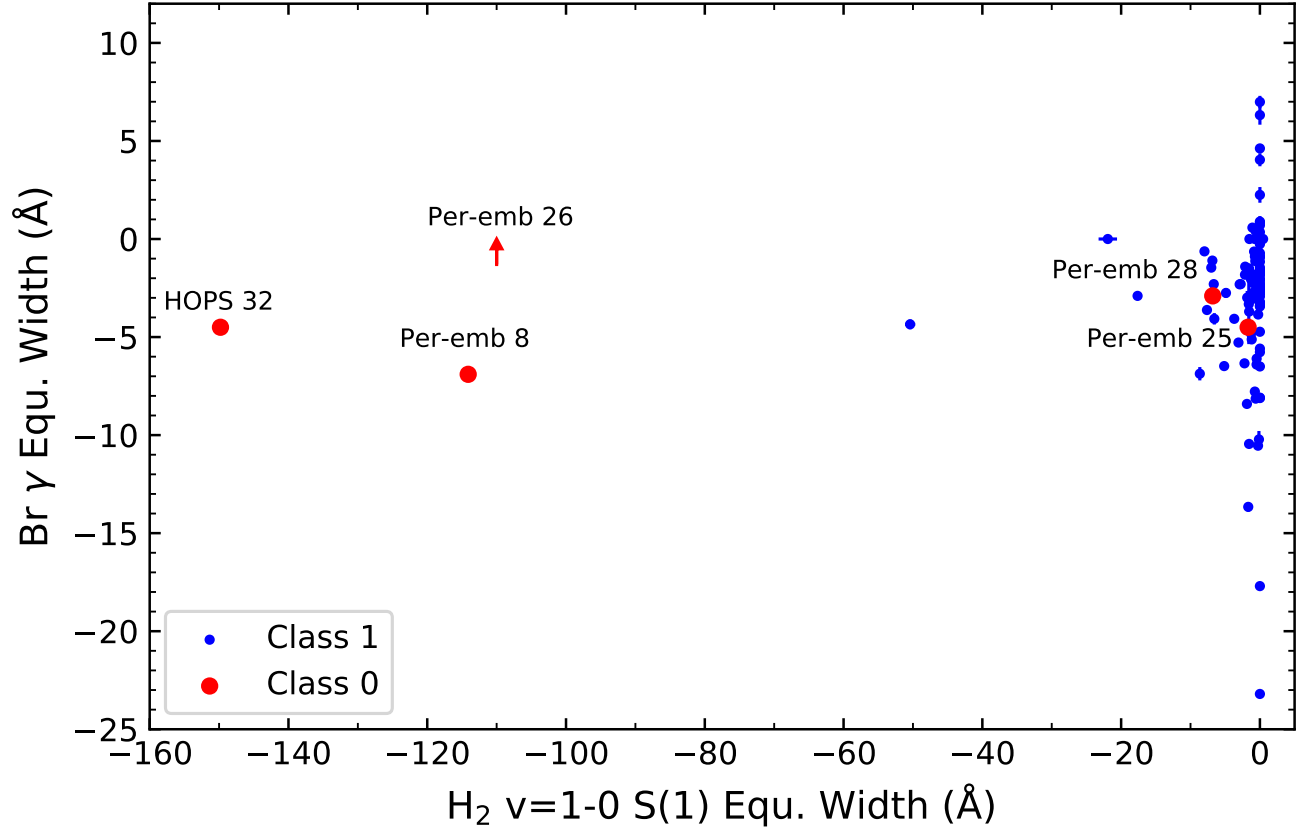


Figure 5. Br γ equivalent widths vs. H₂ v=1-0 S(1) equivalent widths. Red points correspond to observed Class 0 sources (this work) while blue points correspond to observed Class I sources (Connelley & Greene 2010). Undetected lines are represented with arrows, corresponding to 3σ upper limits. We find some of our Class 0s exhibit significantly higher H₂ v=1-0 S(1) EWs than this sample of Class Is (Section 3.3).

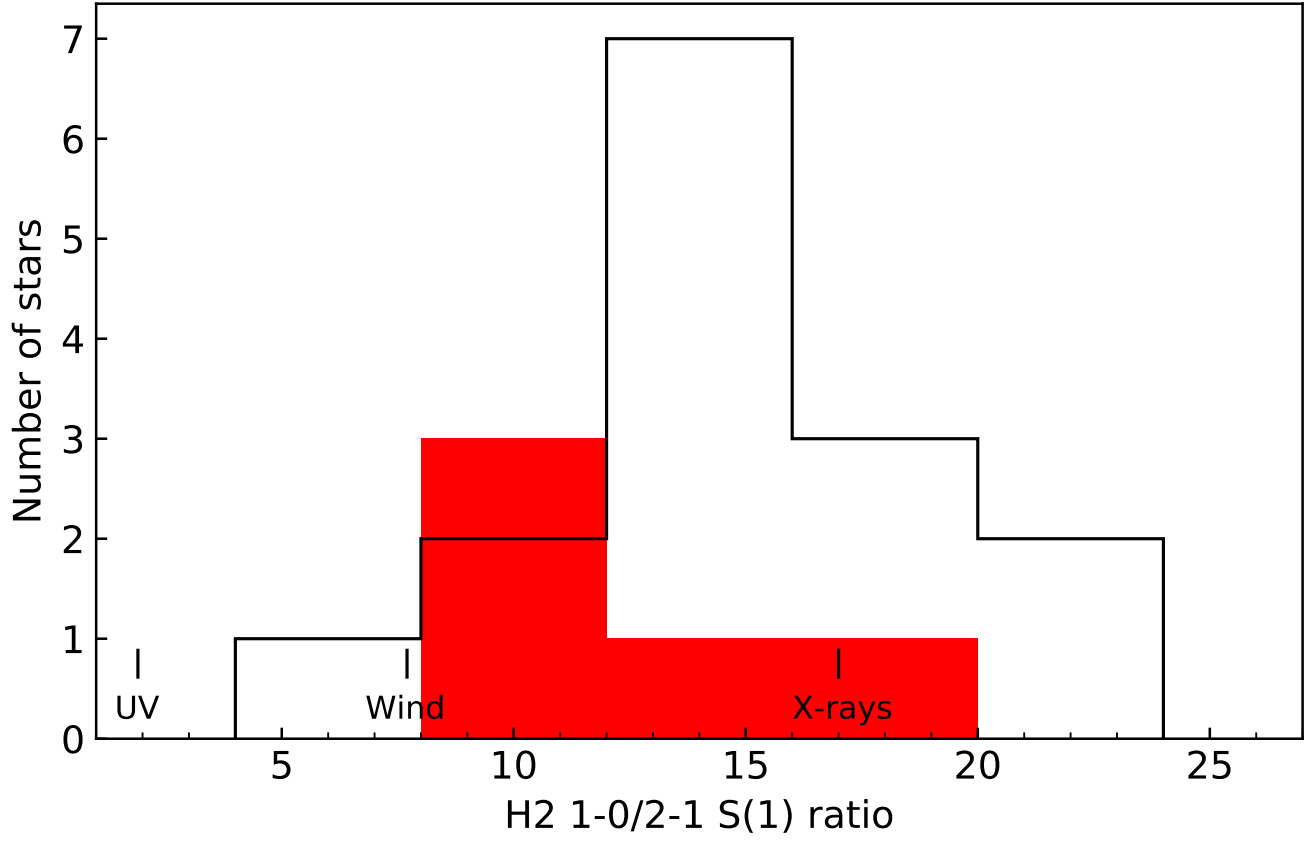


Figure 6. Histogram of $\text{H}_2 \nu = 1-0/2-1 S(1)$ line ratios between our Class 0s (red) and the Class Is observed in [Greene et al. \(2010\)](#) (black). We find the line ratios of our Class 0s argue in favor of shocks in a wind or X-rays as the most likely H_2 source excitation mechanism.

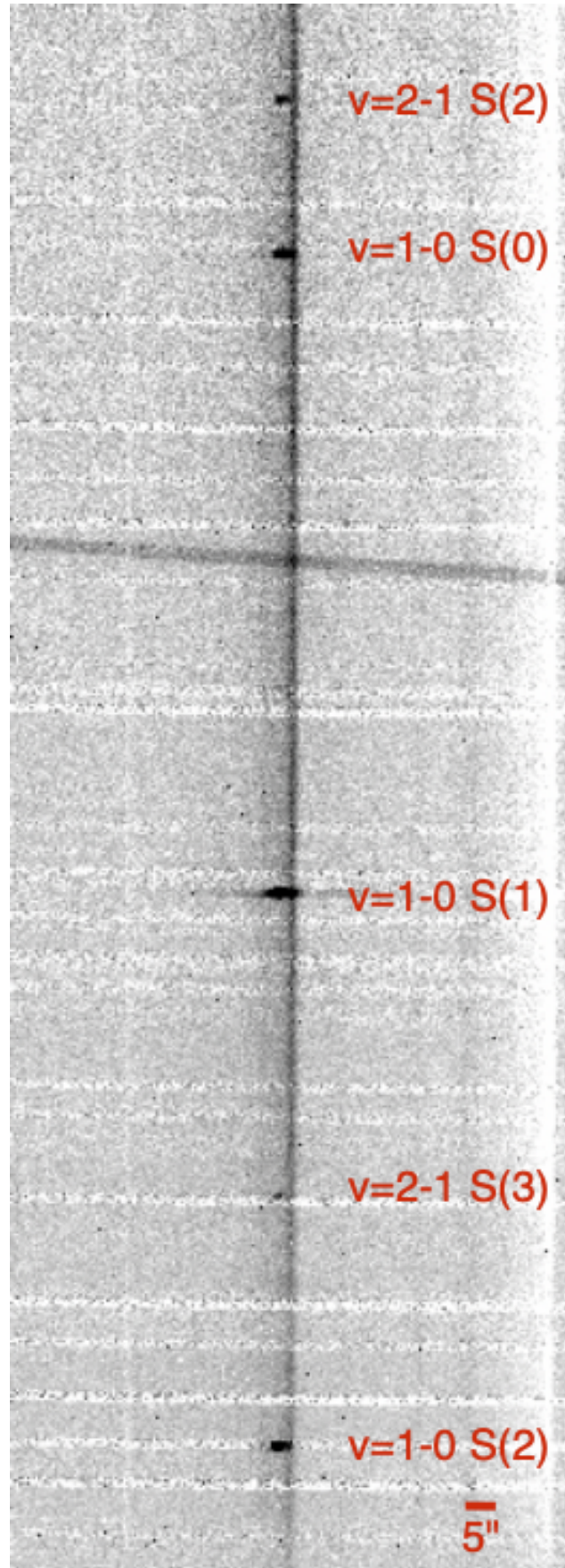


Figure 7. An example of the extended H₂ emission seen in our reduced 2d spectral images. The frame cut is centered on the observed continuum of Per-emb 8 from a single 120s exposure observed on UT date 2019 October 14. We label the individual features and discuss the slit position angle (PA) alignment with the PA of known outflows in Section 3.4.

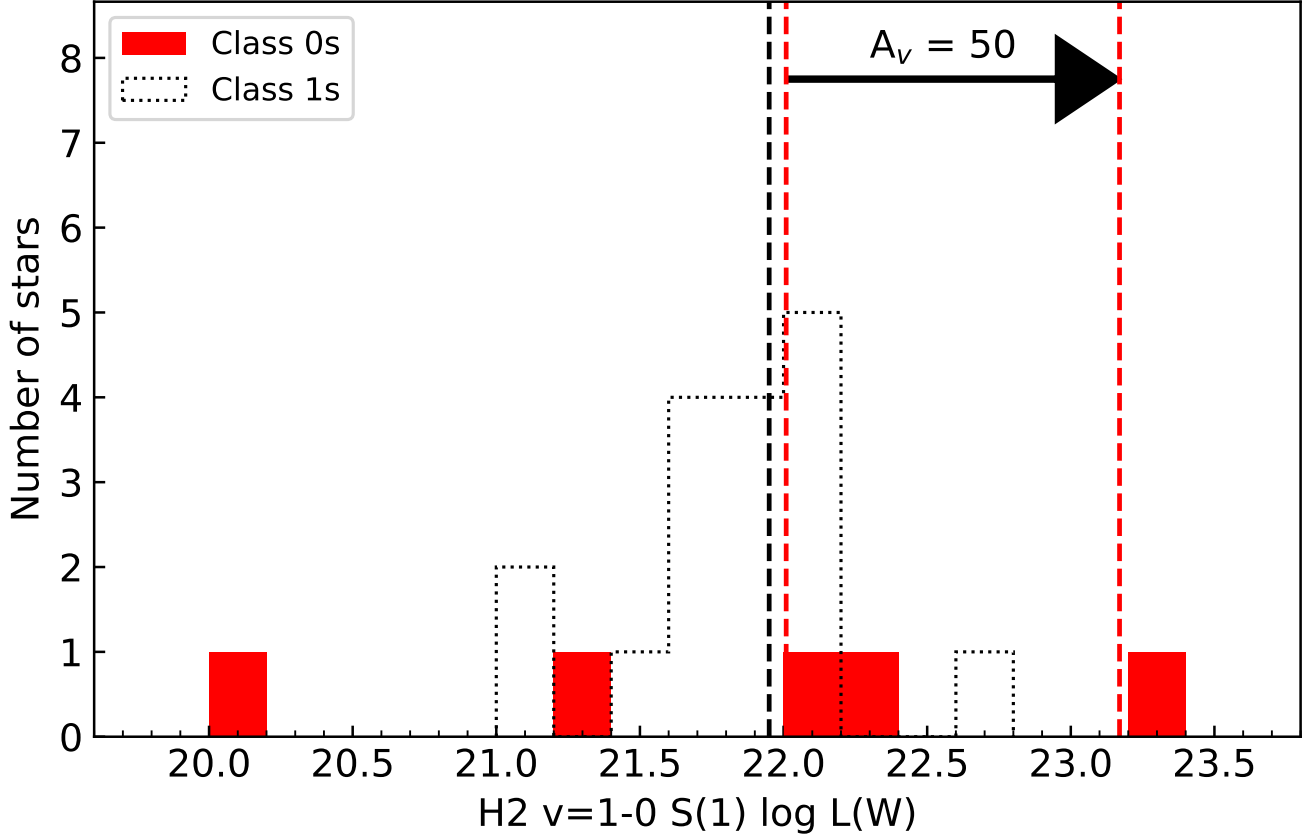


Figure 8. Histogram of H₂ ν = 1-0 S(1) line luminosities between our Class 0s (red) and the Class 1s observed in [Greene et al. \(2010\)](#) (black). We note our Class 0 line luminosities have high uncertainties (Section 3.5); the visual extinctions derived for de-reddening are likely underestimated given the complicated physical nature of our Class 0s (e.g. non-symmetrical envelopes, scattered light). We indicate the median H₂ ν = 1-0 S(1) line luminosity for the Class 1 sample (vertical dashed black line). In red, we also indicate this median value for our Class 0 line luminosities (vertical red dashed line) after de-reddening by the extinction estimates from our SED fitting (left) or by an effective extinction of 50 magnitudes for all of our Class 0 sources (right). More precise Class 0 extinction estimates are needed to determine the extent to which the H₂ line luminosities of Class 0 and I sources differ.

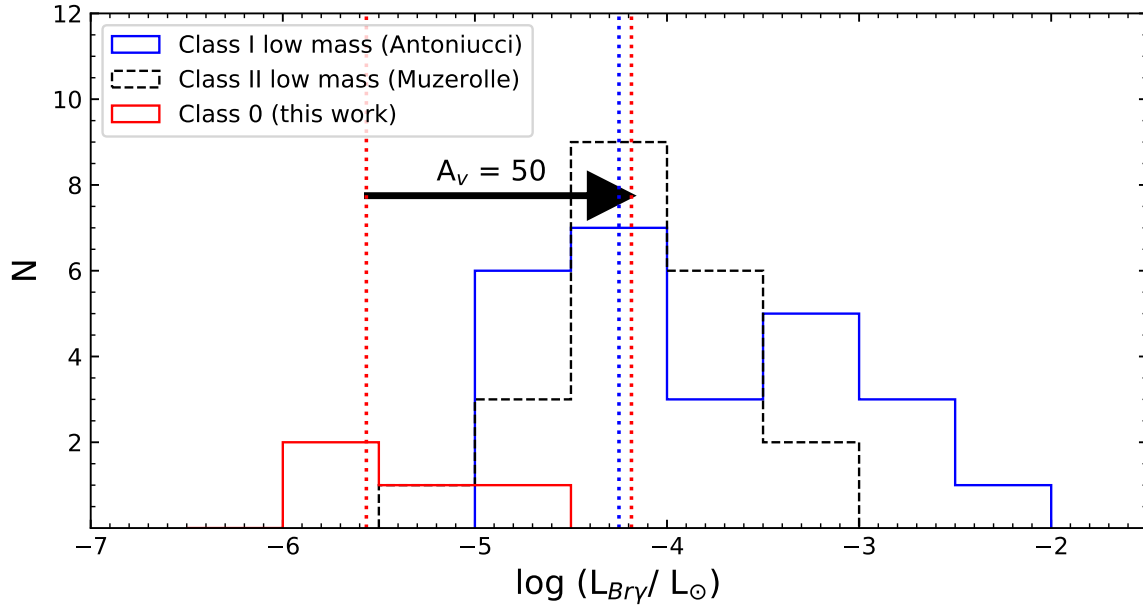


Figure 9. Histogram of Br γ line luminosities between our Class 0s (red), low mass Class Is (Antoniucci et al. 2008) (blue), and low (Muzerolle et al. 1998) mass Class IIs (black). As in Figure 8, we note our Class 0 line luminosities have high uncertainties (Section 3.5). We indicate the median Br γ line luminosity for the Class I and II samples (vertical dashed blue line). In red, we also indicate this median value for our Class 0 line luminosities (vertical red dashed line) after de-reddening by the foreground extinction estimates from our SED fitting (left) or by an effective extinction of 50 magnitudes for all of our Class 0 sources (right). More precise Class 0 extinction estimates are needed to determine the extent to which the Br γ luminosities of Class 0 and I sources differ.

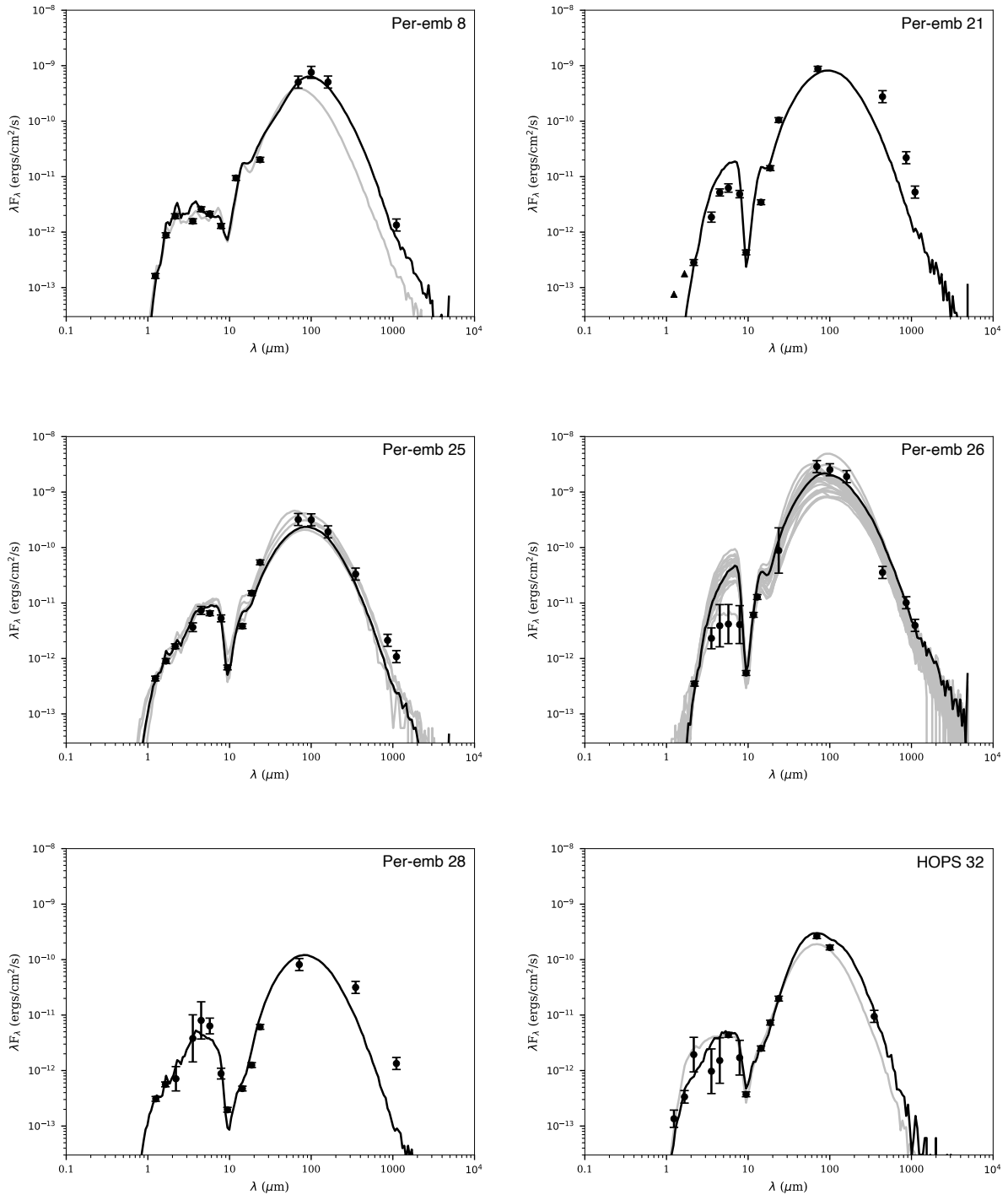


Figure 10. The results of SED fitting for our Class 0 sources using the SED models of [Robitaille et al. \(2006\)](#). We show both the best-fit model (black) and the family of models for which $\chi^2 - \chi^2_{best}$ per data point < 3 (grey). We detail our methodology and interpret these results in Appendix Section A.

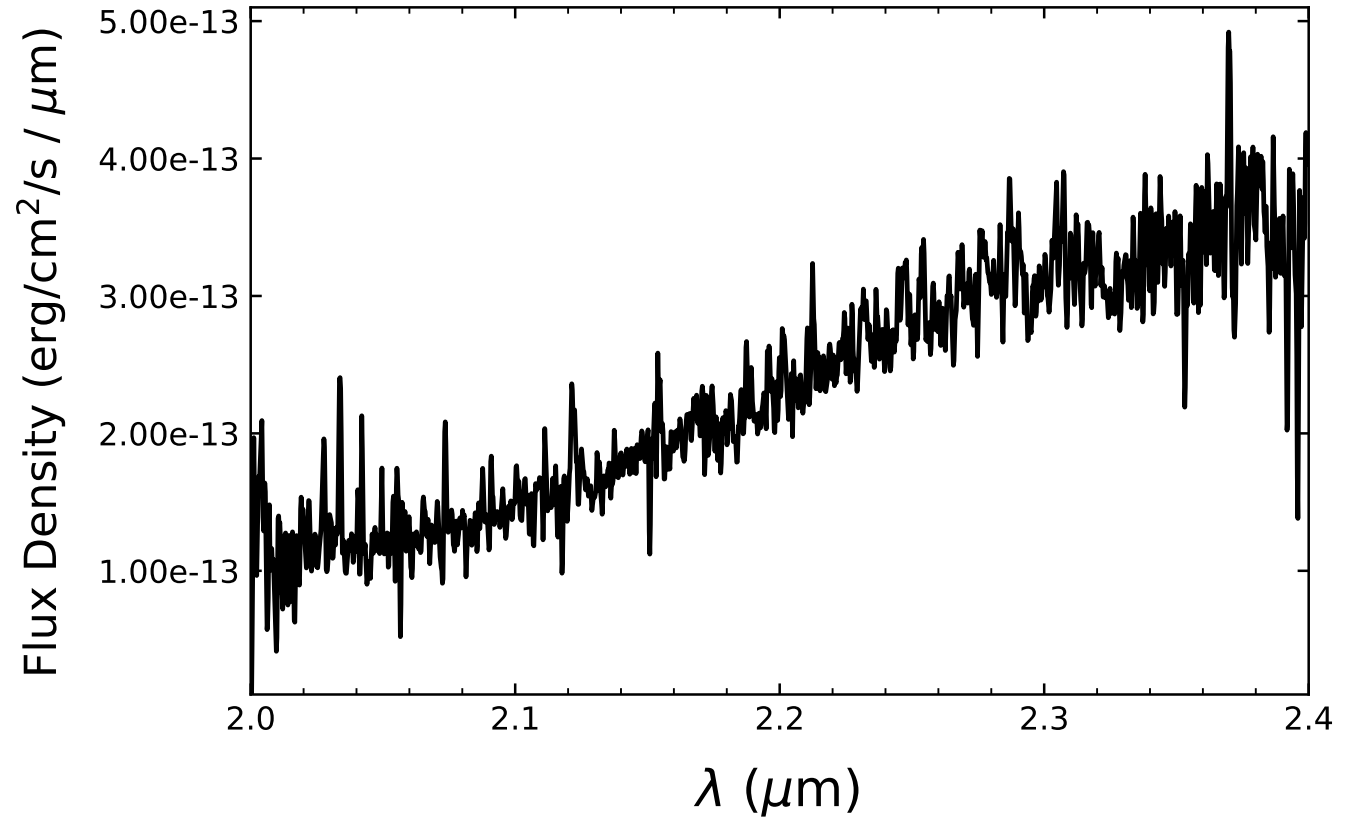


Figure 11. Near-IR MOSFIRE spectrum of HOPS 44 taken on UT Oct 13 for a total integration time of 12 minutes (smoothed by a Gaussian filter for a clearer display). We exclude HOPS 44 from the final sample of Class 0 we analyze in Section 3 due to the low S/N of its observation (Appendix Section B).

Table 6
Derived Parameters from Best-fit SED Models

	A_v^a	i^b	\dot{M}^b	M_c^b	M_{env}^b
	mag	deg	M_\odot/Myr	M_\odot	M_\odot
Per-emb 26	18.7	32	2.10E-04	7.40E-01	19.7
Per-emb 25	9.3	32	5.90E-05	2.50E-01	8.20E-01
Per-emb 21	36.4	32	1.40E-04	4.70E-01	5.50E+00
Per-emb 28	4.7	49	2.80E-05	1.90E-01	3.10E-01
Per-emb 8	20.9	18	7.80E-05	2.00E-01	3.90E+00
HOPS 32	23.9	87	3.60E-06	2.65E+00	2.20E-01

^aThese very approximate, likely lower, foreground extinction estimates were computed with the goal of de-reddening our line luminosities (see Section 3.5, Appendix Section A).

^bWe note these parameters are estimates with large uncertainties from our SED fitting procedure. In some cases, these values likely differ significantly from the true value for the system. Subsequently, they are not used in the analysis of this work and should be considered with care.